Newsletters on Stratigraphy, Vol. 55/3 (2022), 361–384
Published online January 13, 2022; published in print June 2022

Late Paleocene to middle Eocene carbon isotope stratigraphy of the Northern Negev, Southern Israel: potential for paleoclimate reconstructions

Chris D. Fokkema[1]*, Sophie Buijs[2,3], Or M. Bialik[4,5], Aaron Meilijson[5], Nicolas D. Waldmann[5], Yizhaq Makovsky[5], Joost Frieling[1,6], Gerald R. Dickens[7] and Appy Sluijs[1]

With 9 figures and 1 table

Abstract. Sedimentary records depicting significant variability in climate and carbon cycling across the early Paleogene have emerged over the last two decades. Continuous, long-term, high-resolution records mostly derive from deep-sea drill cores, and only few derive from continental margin locations. Here we examine lower Paleogene marls and chalks collected from a core (RH-323) in the Northern Negev Desert (Southern Israel). The studied sediments accumulated on a continental slope of the southern Tethys at ~500–700 m paleodepth and did not undergo deep burial. We analyzed bulk carbonate stable carbon and oxygen isotopes and bulk magnetic susceptibility. The resulting records can be aligned with those from elsewhere and include the Paleocene Carbon Isotope Maximum (PCIM), Paleocene Eocene Thermal Maximum (PETM) and Early Eocene Climatic Optimum (EECO). An obvious realization is a concurrence between local lithological variations and major climate and carbon cycle changes. This has been highlighted for sedimentary sequences elsewhere, but the relations differ in the Negev, such that carbonate rich intervals mark the PCIM and PETM, and a transition from marl to chalk initiates the EECO. Overall, the relatively pristine and immature sediment records in southern Israel likely provide potential for high-resolution paleoclimate and carbon cycle reconstructions during a crucial time interval and in a crucial part of the world.

Key words. Early Paleogene, carbon isotope stratigraphy, Revivim Valley, Northern Negev, Southern Tethys margin, bulk carbonate

Authors' addresses:
[1] Department of Earth Sciences, Faculty of Geosciences, Utrecht University, Princetonlaan 8, 3584CB Utrecht, The Netherlands; c.d.fokkema@uu.nl, a.sluijs@uu.nl
[2] Faculty of Science, Universiteit van Amsterdam, Science Park 904, 1098XH Amsterdam, The Netherlands
[3] Faculty of Science, Vrije Universiteit, Boelelaan 1085, 1081HV Amsterdam, The Netherlands
[4] (Present address): Department of Geosciences, Faculty of Science, University of Malta, Msida MSD 2080, Malta; o.bialik@campus.haifa.hc.il
[5] Dr. Moses Strauss Department of Marine Geosciences, The Leon H. Charney School of Marine Sciences, University of Haifa, Mt. Carmel, Haifa 3498838, Israel; o.bialik@campus.haifa.hc.il, ameilijs@campus.haifa.ac.il, nwaldmann@univ.haifa.ac.il, yizhaq@univ.haifa.ac.il
[6] (present address): Department of Earth Sciences, University of Oxford, South Parks Road, Oxford, OX1 3AN, United Kingdom; joost.frieling@earth.ox.ac.uk
[7] Department of Geology, School of Natural Sciences, Trinity College, Dublin 2, Ireland; dickensg@tcd.ie
* Corresponding author: c.d.fokkema@uu.nl

DOI: 10.1127/nos/2022/0684 Borntraeger Science Publishers, Stuttgart, www.borntraeger-cramer.com

1. Introduction

1.1. Long-term climate and carbon cycle trends of the Paleogene

Millennial-scale deep-ocean benthic foraminifera oxygen ($\delta^{18}O$) and stable carbon isotope ($\delta^{13}C$) records (Fig. 1) show long-term trends and short-term perturbations across the early Paleogene (e. g., Westerhold et al. 2020). In the absence of large continental ice sheets, variability in benthic $\delta^{18}O$ dominantly reflects changes in surface temperature at high-latitudes, where deep water forms (Zachos et al. 2001). The temperature trends captured by the benthic $\delta^{18}O$ signal broadly correspond with those inferred from other (surface) paleotemperature indicators, including fossil assemblages (Bijl et al. 2011, Luciani et al. 2016, Crouch et al. 2020), organic biomarkers (Bijl et al. 2009, Cramwinckel et al. 2018, Crouch et al. 2020), and the geochemical composition of planktonic foraminifera (Evans et al. 2018) and bulk biogenic carbonate (Zachos et al. 2010). These trends strongly suggest that long-term warming commenced in the late Paleocene (~59 Ma) and culminated in a prolonged hothouse climate state (Shackleton et al. 1984), now coined the Early Eocene Climatic Optimum (EECO; ~53–49 Ma; Zachos et al. 2001, Westerhold et al. 2018). After the EECO, temperatures generally cooled through the rest of the Eocene.

Secular variations in benthic foraminiferal $\delta^{13}C$ also appear in $\delta^{13}C$ records of planktonic foraminifera and bulk carbonate (Shackleton et al. 1984, Shackleton 1986, Hollis et al. 2005, Zachos et al. 2010). As such, they reflect changes in net carbon fluxes to and from the exogenic carbon cycle (Shackleton 1986, Kump and Arthur 1999). Across the early Paleogene, the rises and falls in $\delta^{13}C$ likely relate to storage and release of ^{13}C-depleted organic carbon (Kurtz et al. 2003, Hilting et al. 2008, Komar et al. 2013). On the multi-million-year timescale (Fig. 1), a gradual $\delta^{13}C$ increase starts in

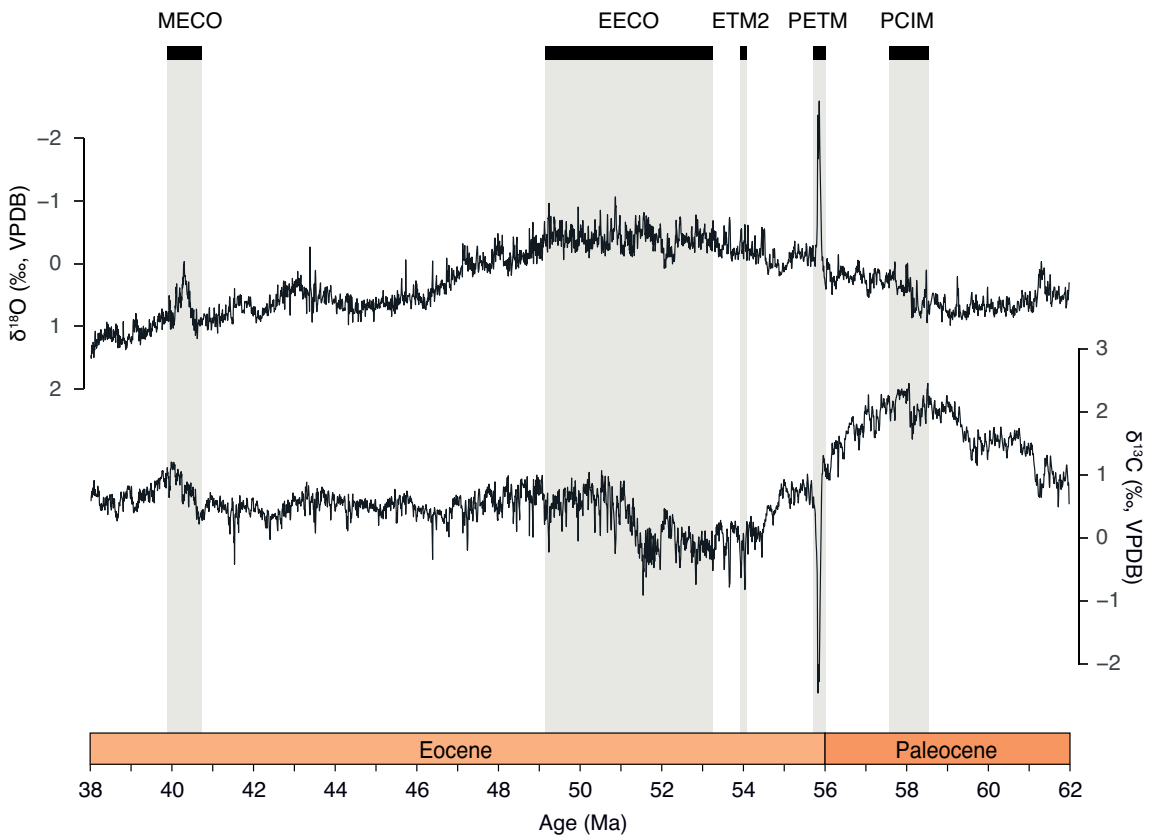

Fig. 1. Compilation of early Paleogene deep ocean benthic foraminifer oxygen and carbon isotope records. Grey boxes indicate intervals of enhanced warmth, marked carbon cycle perturbations, or both. PCIM = Paleocene Carbon Isotope Maximum; PETM = Paleocene Eocene Thermal Maximum; ETM2 = Eocene Thermal Maximum 2; EECO = Early Eocene Climatic Optimum; MECO = Middle Eocene Climatic Optimum. Data comes from compilation by Westerhold et al. (2020).

the middle Paleocene and ends with the Paleocene Carbon Isotope Maximum (PCIM). This is followed by a major 2.0–2.5‰ drop toward the EECO with a subsequent ~1‰ rise during peak-EECO warmth (Shackleton et al. 1984, Shackleton 1986, Zachos et al. 2001, Luciani et al. 2016, Lauretano et al. 2018).

1.2. Transient early Paleogene climate and carbon cycle perturbations

Superimposed on the long-term climate and carbon cycle trends of the early Paleogene were shorter (~100 kyr) episodes of global warming, biological change and carbon cycle upheaval (Thomas and Zachos 2000, Cramer et al. 2003, Lourens et al. 2005, Nicolo et al. 2007, Zachos et al. 2008, Speijer et al. 2012). These events, referred to as hyperthermals, manifest as transient negative $\delta^{18}O$ and $\delta^{13}C$ excursions, as well as enhanced carbonate dissolution horizons in the deep-sea (Zachos et al. 2005, Lourens et al. 2005, Sluijs et al. 2007, Sluijs et al. 2009, Agnini et al. 2009, Stap et al. 2009, Stap et al. 2010, Kirtland Turner et al. 2014, Lauretano et al. 2018, Westerhold et al. 2018). The most prominent hyperthermal was the Paleocene Eocene Thermal Maximum (PETM; 56 Ma), marked in benthic foraminifera records by a 1.5–2.5‰ negative $\delta^{18}O$ excursion and a 2–4‰ negative $\delta^{13}C$ excursion, or CIE (Kennett and Stott 1991, John et al. 2008, McCarren et al. 2008, McInerney and Wing 2011). Increased terrigenous sediment accumulation rates at multiple locations along continental margins during the PETM suggest an acceleration of the hydrological cycle and enhanced erosion on land (Sluijs et al. 2014, Carmichael et al. 2017 and references therein).

1.3. Research aim

Long-term trends and transient perturbations in climate and carbon cycling during the early Paleogene have become a major research focal point. Among current issues are two that propel this research. First, most continuous, long-term records of the early Paleogene derive from sequences deposited in the Atlantic and Pacific (overview in Hollis et al. 2019). By contrast, relatively few records exist for the Tethyan realm, especially east of present-day Italy. Yet, this region, which connected the Atlantic and Pacific (Fig. 2a), potentially played an important role in early Paleogene atmospheric and zonal ocean circulation (e. g., Hotinski and Toggweiler 2003). Secondly, continuous long-term sedimentary records mainly derive from open ocean sites; expanded and continuous continental margin records are rare due to their intrinsic irregular sedimentation and are often diagenetically compromised or deeply buried. Nonetheless, the few available lengthy early Paleogene sections that

Fig. 2. Maps showing locations mentioned in the text. a) Paleogeographic positions of drillsite RH-323 in the northern Negev desert (red dot) and other localities discussed in the text (white dots) at 56 Ma. The map is generated with GPlates (Boyden et al. 2011) based on the plate reconstruction by Seton et al. (2012), following the paleomagnetic reference frame of Torsvik et al. (2012). Continents (white) are surrounded by modern coastlines, grey lines indicate reconstructed Paleogene shelf breaks, and grid spacing is 30°. b) Map showing present day positions of the RH-323 drill site and the Ben-Gurion outcrop, along with estimated contours of early Paleogene bathymetry edited from Speijer (1994a). The thick black line represents a generic transect as shown in Fig. 3a

represent continental margin sedimentation, for example those now exposed on South Island, New Zealand (e. g., Hollis et al. 2005, Nicolo et al. 2007, Slotnick et al. 2012), show a clear relation between climate variability and continental hydrology on both short- and long-term scales. Such records remain relatively sparse, especially for margins along arid landmasses, where the hydrological cycle may have differed during past climate change.

Here we begin to address the above two issues by describing and examining an upper Paleocene to middle Eocene succession recovered at a drill site in Revivim Valley of the northern Negev desert, Israel. Sediments within the region accumulated on a southern Tethys slope at a paleolatitude of ~15 °N (Fig. 2a). Previous work on nearby outcrop sections, including microfossil biostratigraphy, has shown lithological variability on various timescales and relatively complete deposition from the late-Paleocene through the middle Eocene (Romein 1979, Benjamini 1980a, Weinbaum-Hefetz and Benjamini 2011). Because regional uplift began in the late Eocene (Segev et al. 2011), the early Paleogene succession was never buried deeply.

2. Regional lithology and stratigraphy

Early Paleogene strata across the Levant mostly consist of marls and chalks with intermittent cherts (Speijer 1994b, Ziegler 2001). These sediments were deposited on the southern margin of the Tethys in settings ranging from outer neritic (<100 m water depth) in southeast Egypt to bathyal (>500 m) in northeast Egypt and southern Israel (Speijer 1994b) (Fig. 2b). Since the late Paleocene, regional clay mineral composition is generally dominated by palygorskite, sepiolite and smectite, suggestive of warm and dry conditions along much of the southern Tethys margin that peak during the early Eocene (Bolle et al. 2000). In the northern Negev, geologists (Bentor and Vroman 1960) divide the upper Paleocene to middle Eocene strata into six formations (Fig. 3a).

The Paleocene Taqiye Formation (Fm) consists of chalk-clay marls that typically span ~50–100 m of stratigraphic thickness. A ~5–20 m thick chert-bearing calcareous interval, referred to as the Hafir Member (Mbr), interrupts the top Taqiye Fm in many locations (Bentor and Vroman 1960). The base of the Hafir Mbr is dated by calcareous nannofossils and planktonic foraminifera to the to NP7-8 and P4 biozones, respectively (Romein 1979, Charisi and Schmitz 1995, Charisi and Schmitz 1998, Schmitz et al. 1997). This age corresponds to a maximum flooding surface (Pg10) across the Arabian Platform (Sharland et al. 2001).

Carbonate content gradually increases above the Hafir Mbr and fully transitions to chalk within the Ypresian (Bartov et al. 1972). This lithological change is diachronous, occurring between calcareous nannofossil biozones NP10 and NP12, but generally starting earlier in the north (Weinbaum-Hefetz 2013). The Ypresian chalk facies contains numerous chert horizons and is referred to as the Mor Fm in southern Israel and the Adulam Fm in northern Israel. Within the upper Mor Fm, several bituminous horizons (up to 10 cm) occur (Romein 1979). Like other regional lithostratigraphic units, the thickness of the Mor Fm varies spatially, from being absent to more than 60 m thickness (Benjamini 1980a).

The overlying Nizzana Fm, of late Ypresian and early Lutetian age, is characterized by decreasing chert abundance and more prevalent mass transport deposits. This formation consists of thin to thick bedded, dark yellow-brown chalks and limestones with occasional flint concretions (Bartov et al. 1972, Weinbaum-Hefetz and Benjamini 2011). The base of the Nizzana Fm, marked by high abundances of large benthic foraminifera, closely corresponds to the base of calcareous nannofossil biozone NP13 (Romein 1979, Weinbaum-Hefetz and Benjamini 2011). The total thickness of the unit typically varies between 50 and 100 m (Benjamini 1980a).

Chert disappears in the middle Lutetian, a lithological change that heralds two additional formations. A ~45 m thick sequence of white, massive chalks, termed the Horsha Fm, overlies the Nizzana Fm (Weinbaum-Hefetz and Benjamini 2011). Above this lies the upper Lutetian-Bartonian Matred Fm, marked by more indurated yellowish chalks and a reoccurrence of mass transported beds (Bartov et al. 1972, Weinbaum-Hefetz and Benjamini 2011). Honigstein et al. (2002) report a typical thickness of 65 m for the Matred Fm.

A transition toward marl-rich deposits in the upper-middle Eocene to upper Eocene is associated with the base of the Qeziot Fm in southern Israel and the Bet Guvrin Fm elsewhere in Israel (Benjamini 1980b, Gvirtzman 2004, Gvirtzman et al. 2011). Approximately at this time, the long period of relative tectonic quiescence ended with initiation of regional uplift (Segev et al. 2011).

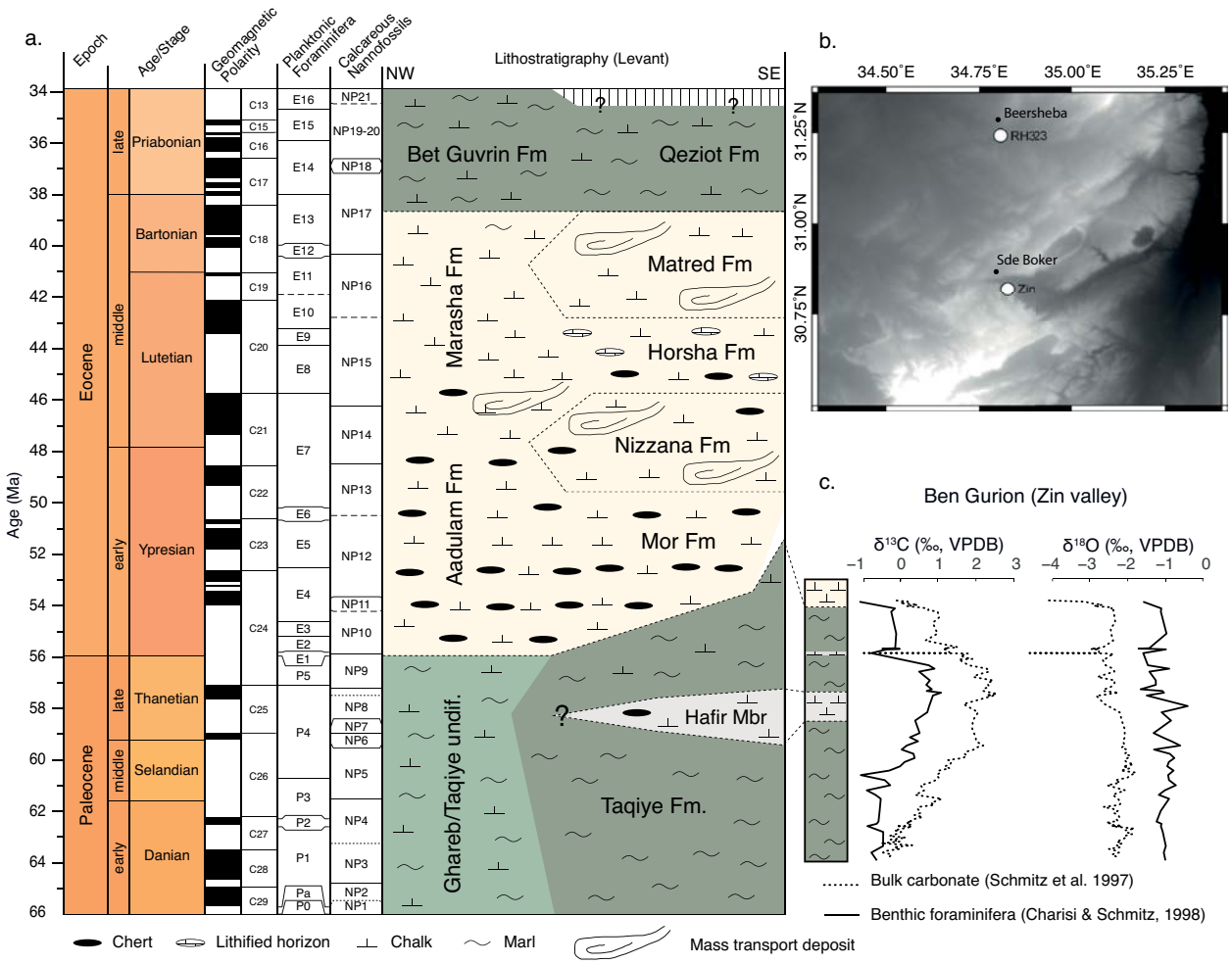

Fig. 3. Regional lithostratigraphy and isotope results from Zin Valley. a) The global low-latitude Paleocene-Eocene stratigraphic framework (Gradstein et al. 2012) with the regional lithostratigraphy from the northern Negev (SE) to the western Galilee region (NW) along the transect approximately depicted in Figure 2b. b) Topographic map (lighter = higher) indicating positions of Zin Valley, which includes the Ben Gurion section, and Revivim Valley, which hosts the RH-323 drill site. c) Stable isotope records of bulk carbonate (dotted lines) and benthic foraminifera (solid lines) from the Ben Gurion outcrop section plotted against the lithostratigraphic framework of Figure 3a supported by biostratigraphic age control (Schmitz et al. 1997, Charisi and Schmitz 1998).

Revivim and Zin valleys (Fig. 3b) were early Paleogene bathymetric depressions along SW-NE striking synclines part of the Syrian Arc fold belt and exhibit differential fill patterns (Krenkel 1924, Blanckenhorn 1925, Shahar 1994, Meilijson et al. 2014). The early Paleogene succession in this area accumulated in a pelagic setting on a basinward tilted mid-Cretaceous carbonate ramp at water depths of 500–700 m (Speijer 1994a, Segev et al. 2011). As noted above, several outcropping sections in the region have been dated using calcareous nannofossil and planktonic foraminifer assemblages (Romein 1979, Schmitz et al. 1996, Speijer and Schmitz 1998, Bolle et al. 2000, Weinbaum-Hefetz and Benjamini 2011). Bulk carbonate and foraminifer $\delta^{13}C$ and $\delta^{18}O$ records have been generated from the lower units of the Ben Gurion section (Schmitz et al. 1997, Charisi and Schmitz 1998, Fig. 3c). These show a high in $\delta^{13}C$ values across the Hafir Mbr, which corresponds with the PCIM. In addition, a thin calcarenite layer close to the top of the Taqiye Fm includes the CIE and benthic extinction event associated with the PETM (Schmitz et al. 1997). The link between global carbon cycling and regional lithological variation is intriguing, although stable isotope data remain absent for much of the Eocene in the region. Moreover, the predominance of chalk, rather than limestone, suggests a setting suitable for paleoclimatological reconstructions.

3. Material and Methods

3.1. Material

Core RH-323 (31.143°N, 34.798°E; Figs. 2, 3) was retrieved as part of a hydrogeological survey in Revivim Valley southern Israel (Adar et al. 1999) and was made available for this study. The core spans nearly 350 m of upper Paleocene to middle Eocene strata, chronologically constrained by calcareous nannofossil and planktonic foraminifer biostratigraphy (Eshet and Siman-Tov 2000).

A set of 116 samples was selected from Sections 1–77 of Core RH-323 (Table S1). Samples span an interval between ~93 m to 345 m below land surface (mbs). The upper sections were not sampled due to time limitation and because some had a crumbly nature related to pedogenesis. Sampling resolution averaged approximately 3 m, but varied between 0.05 and 6.65 m to capture certain lithological transitions and to avoid chert-rich intervals (see core examples and preservation states in Fig. 4).

3.2. Methods

3.2.1. Magnetic susceptibility analysis

Subsamples averaging 30 cm^3 were taken from the core sections using a hammer and chisel. Each sample was scraped clean, freeze-dried overnight and crushed by mortar and pestle. Each subsample was analyzed for mass-specific bulk magnetic susceptibility (MS) at

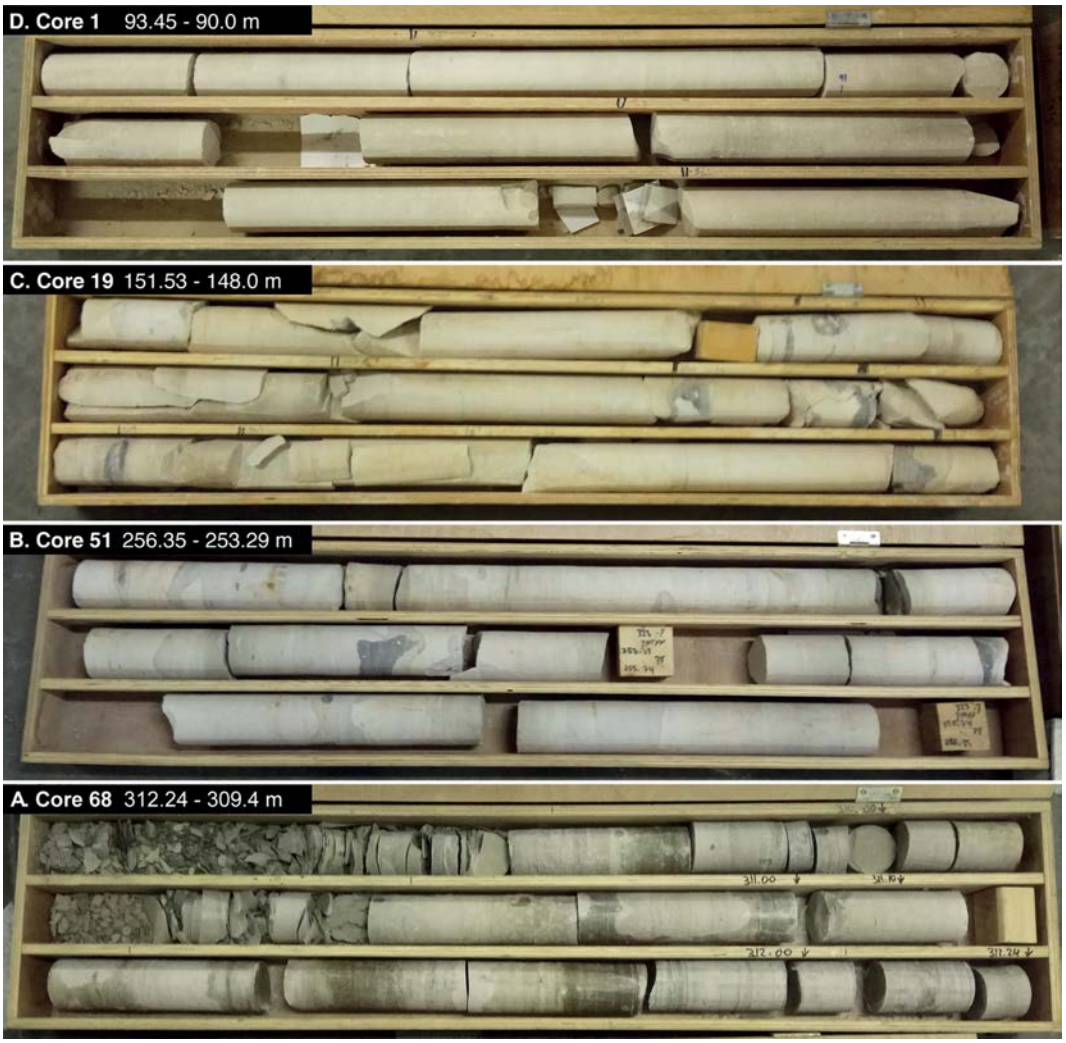

Fig. 4. Four examples of studied RH-323 cores. a) grey-green marl (312.24–309.4 m depth) b) white chalk with darker chert nodules (256.35–253.29 m depth) c) yellowish chalk with some darker chert nodules (151.53–148.0 m depth) d) homogenous light cream colored chalk (93.45–90.0 m depth).

Utrecht University with a Multi-Function Kappabridge (MFK1-FA), with values reported in χ. MS values of discrete samples were compared to published high-resolution data generated by a Multi Sensor Core Logger (MSCL) at Haifa University (Opuwari et al. 2021). To enable comparison with the discrete dataset, values from the MSCL were converted from volume-specific MS to mass-specific MS by dividing by density.

3.2.2. Stable isotope analysis

For stable isotope measurements, a powdered aliquot of each sample (between 98 and 420 μg) was weighed and analyzed on a Thermo Finnigan GasBench II system coupled to a Thermo Delta-V mass spectrometer at Utrecht University over two runs. Measurements that exhibited a *m/z* 46 peak higher than 200 mV, indicative of leakage, were re-analyzed in two additional runs. Results were calibrated against an in-house carbonate standard "NAXOS" and the international atomic energy agency carbonate standard "IAEA-CO-1". All values are reported in standard delta notation relative to Vienna Pee Dee Belemnite (VPDB). The maximum standard deviations, based on repeated measurements of NAXOS, were 0.076‰ for $\delta^{18}O$ and 0.093‰ for $\delta^{13}C$.

3.2.3. Approximation of calcium carbonate content

Mineralogical analysis of a selected subset of samples (using a Rigaku MiniFlex XRD with a Cu source at the University of Haifa) shows that low Mg calcite completely dominates the carbonate phase. Thus, a linear regression model between mass-spectrometer *m/z* 44 peak intensity and sample mass (representing a theoretical 100 % carbonate line) was used to estimate carbonate content. Carbonate weight percentage (wt%) of each sample was calculated using slope (a) and intercept (b) of the regression line:

$$CaCO_3(wt\%) = \frac{m/z44\ intensity}{(a * mass + b)} * 100\%$$

For this method, it was assumed that standards consist of 100 wt% $CaCO_3$, and non-$CaCO_3$ components in samples give a *m/z* 44 peak intensity of 0 mV. Across different analytical runs, slopes of regression lines varied (Fig. S1). Precision is assessed from the standard deviation of carbonate weight percentages of the standards across the first two runs, which were 3.6 wt% and 5.8 wt%, respectively

3.3. Biostratigraphic age model

Calcareous nannofossil and planktonic foraminifera biostratigraphic datums have been reported previously for Core RH-323 (Eshet and Siman-Tov 2000). For planktonic foraminifera, we suggest that poor preservation prevents precise age assignment. For calcareous nannofossils, initially established ages were recalibrated to refined ages (Agnini et al. 2014, Westerhold et al. 2017) on the Geomagnetic Polarity Time Scale (GPTS) of 2012 (Gradstein et al. 2012). We prefer this over the GPTS2020 (Ogg 2020) because it is consistent with the recent astronomically calibrated benthic foraminifer isotope compilation (Westerhold et al. 2020). Biostratigraphic age control, using nannofossil datums, spans from the base of NP7 and 58.97 Ma (FO of *Discoaster mohleri*) at 338 mbs to the top of NP12 and 50.66 Ma (LO of *Tribarchiatus orthostylus*) at 225 mbs.

4. Results

4.1. Core lithology

The lithology varies through the studied section (Fig. 5). The lowermost interval consists of grey to green marls up to 296 mbs, punctuated by an ~8 m thick grey to white chalk horizon (~337–329 mbs). White to grey-white chalk overlays the marl interval after a gradual transition (~296–280 mbs). This chalk unit contains abundant chert concretions with a peak occurrence at ca. 230 mbs. Additionally, sediment color becomes yellower higher up. From 138 mbs toward the top of the studied section, no chert is found and the sediments become light cream.

The MS and $CaCO_3$ content (Fig. 5) mimic the observed lithological variations. High MS values (>5 x 10^{-8} χ) and low $CaCO_3$ content (<50 wt%) characterize the marls, although a noticeable drop in MS and rise in $CaCO_3$ occurs across the 8 m thick chalk horizon. A prominent drop in MS is also recorded at ~310 mbs. At ca. 270 mbs, MS declines to nearly zero and $CaCO_3$ rises to above 60 wt%. Apart from a few small-scale peaks and drops, MS remains close to zero and $CaCO_3$ remains generally high (~90 wt%) above 270 mbs. As shown by linear regression analysis (Fig. 6), there is a significant negative rela-

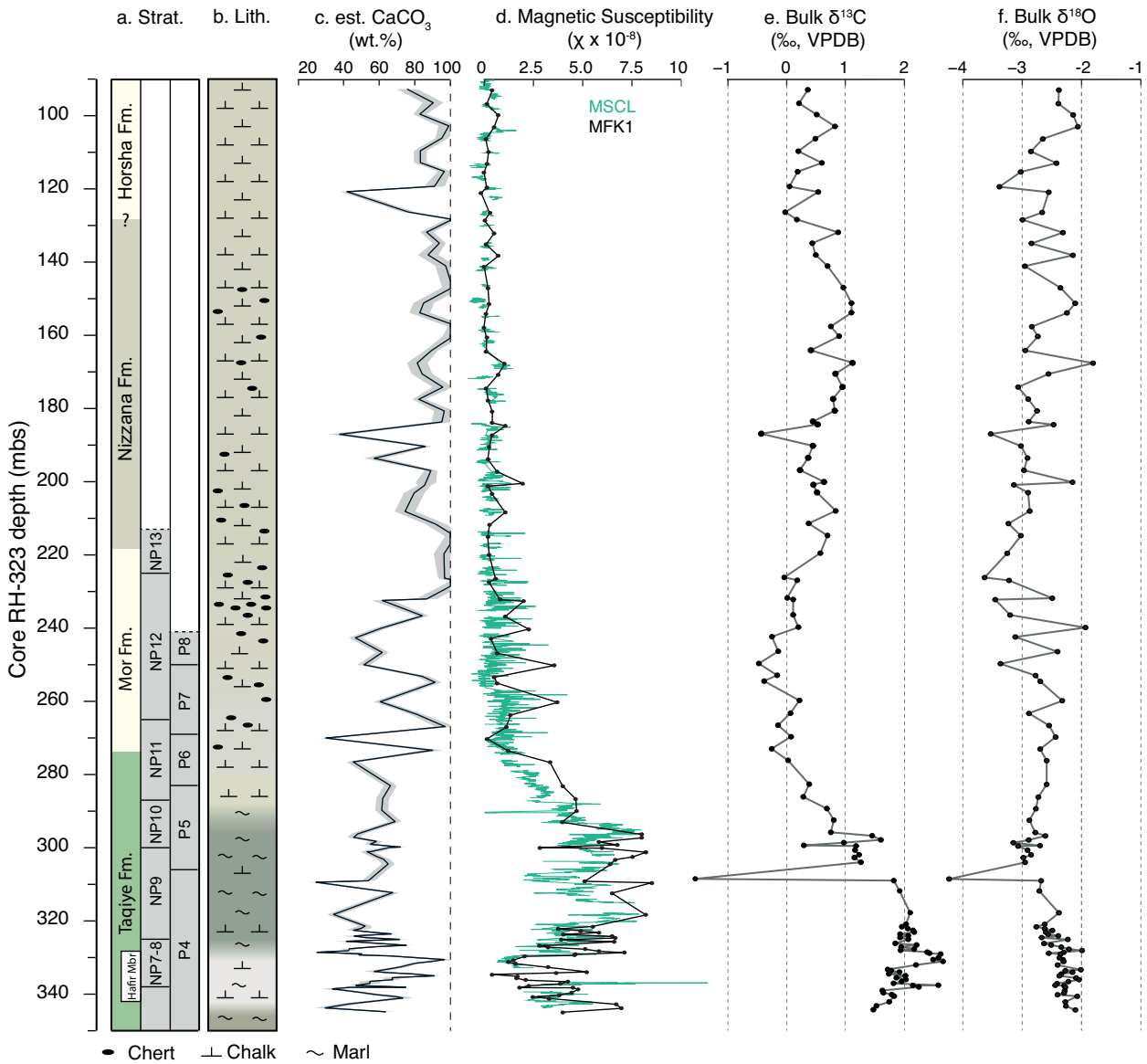

Fig. 5. Downcore results from analysis of Hole RH-323. a) Stratigraphy, including lithostratigraphic units (see Discussion 5.1) and biostratigraphic zonation by Eshet and Siman-Tov (2000). b) General lithology as logged during core sampling. c) estimated wt%$CaCO_3$ with uncertainty (1σ) depicted by grey band (see Material and Methods 3.2.3). d) Magnetic susceptibility measured on discrete samples by MFK1 (black) and continuous with MSCL (green; from Opuwari et al. (2021)). e) Bulk carbonate δ ^{13}C. f) Bulk carbonate $\delta^{18}O$.

tionship between MS and wt%$CaCO_3$ (R^2=0.54, P<0.001). However, this relationship is significantly weaker above 270 mbs (R^2=0.17, P=0.00176) than below this level (R^2=0.36, P<0.001).

4.2. Stable isotopes of bulk carbonate

The lowermost ~40 m of the studied core interval is marked by bulk carbonate $\delta^{13}C$ values above 1.5‰, including two distinct peaks of 2.6‰ and 2.7‰ centered at 338 and 331 mbs, respectively (Fig. 5e). Above the upper peak, $\delta^{13}C$ values generally decrease toward a long-term minimum of –0.5‰ at ~250 mbs. Notably, though, two lows in $\delta^{13}C$ notably punctuate this gradual decline at 309 and 299.8 mbs with values of –1.2 and 0.3‰, respectively. Above, $\delta^{13}C$ values rise toward a maximum of 1.1‰ at 167 mbs, and then generally decrease to values of 0.5 to 1.0‰.

Bulk carbonate $\delta^{18}O$ somewhat mirrors trends in $\delta^{13}C$ (Fig. 5). Values generally decrease from –2.0 to

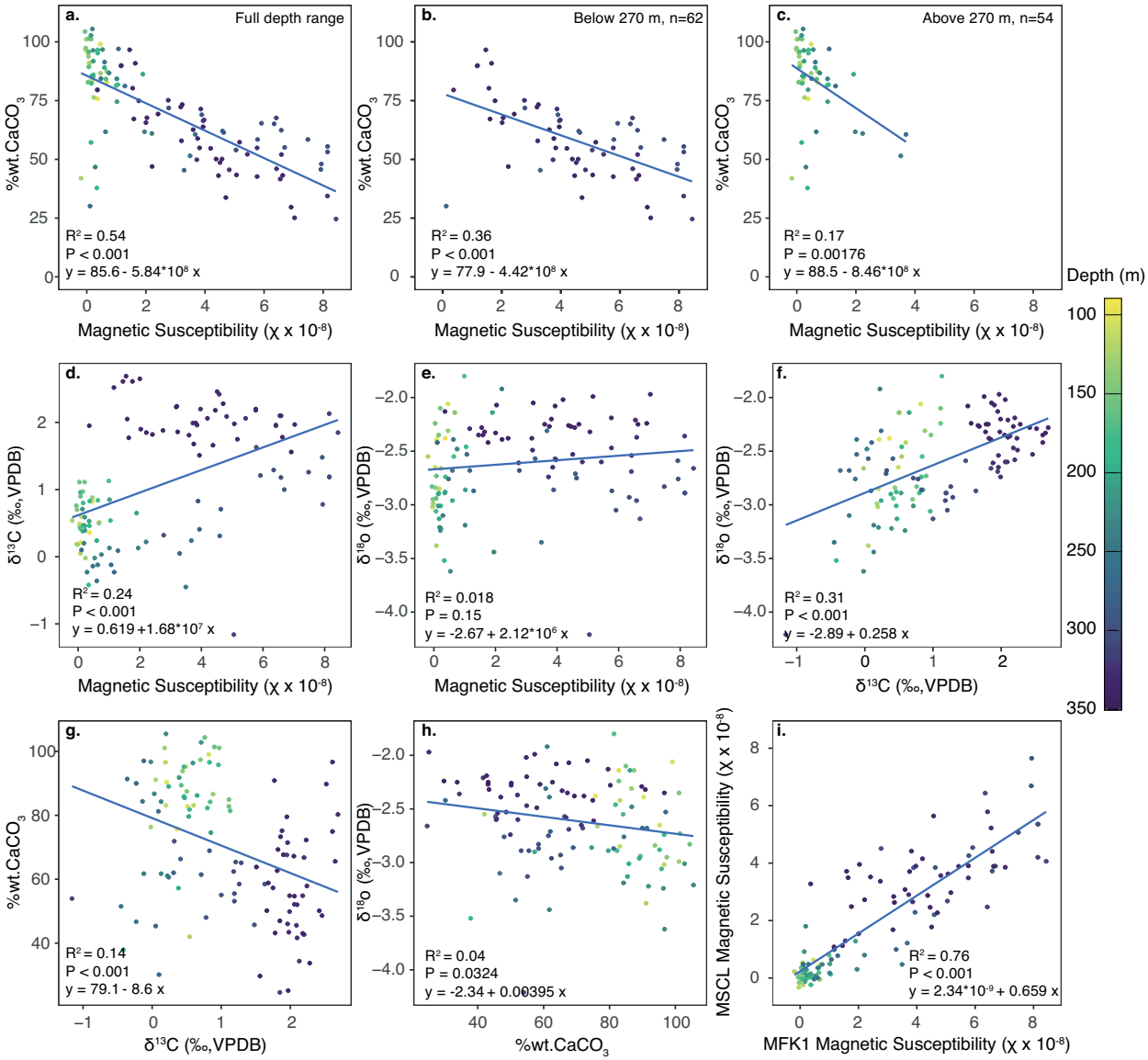

Fig. 6. Cross-plots between the generated datasets. Colors indicate sample depths (mbs), blue lines represent linear regressions, described at the bottom of each panel. n=116 for all plots except b and c. a–c) magnetic susceptibility (MFK1) versus estimated %wt$CaCO_3$, subdivided in the full interval (a), above 270 m depth (b) and below 270 m depth (c). d) Magnetic susceptibility (MFK1) versus $\delta^{13}C$. e) Magnetic susceptibility (MFK1) versus $\delta^{18}O$. f) $\delta^{13}C$ vs $\delta^{18}O$. g) $\delta^{13}C$ versus estimated %wt$CaCO_3$. h) %wt.$CaCO_3$ versus $\delta^{18}O$. i) Magnetic susceptibility measured on discrete samples with MFK1 versus magnetic susceptibility measured by Opuwari et al. (2021) with an MSCL, interpolated to the depths of discrete samples.

–3.5‰ across the lower half of the section. Above ~225 mbs, $\delta^{18}O$ rises by ~1.2‰. One exceptionally low value (–4.2‰) at 309 mbs coincides with the lowest $\delta^{13}C$ value. Across all samples, bulk carbonate $\delta^{13}C$ and $\delta^{18}O$ display a weak but significant positive linear correlation (R^2=0.32) with a regression slope of 0.258 (Fig. 6).

5. Discussion

5.1. Lithology of Core RH-323 in a regional stratigraphical context

The MS signal of bulk sediment samples relates to the relative contribution of para-, ferro- ferri- and imperfect antiferromagnetic components (e. g., magnetite,

Fe-rich clays) versus diamagnetic components (e. g., SiO_2, $CaCO_3$) (Hunt et al. 1995, Liu et al. 2012). In marine sediment, increased MS generally reflects greater presence of detrital grains containing iron-bearing minerals, typically from terrestrial sources (Verosub and Roberts 1995, Liu et al. 2012). Therefore, MS provides a first-order measure of terrigenous material. In combination with wt%$CaCO_3$ and visual core descriptions, the variability in the MS data assists in defining lithological units of different terrigenous and carbonate composition, which when amalgamated with biostratigraphy (Eshet and Siman-Tov 2000) can be assigned to the regional lithostratigraphic units (Fig. 3).

The greenish marl interval at the bottom of the studied core interval (345–296 mbs) (Fig. 4a) which covers biozones NP7-NP11, is identified here as the locally defined Taqiye Fm. A prominent feature within the Taqiye Fm is an ~8 m white calcareous interval (~337–229 mbs), which exhibits low MS values (<2.5 x 10^{-8} χ) and wt%$CaCO_3$ occasionally approaching 100 wt% (Fig. 5). This interval is well-dated within NP7-8 and is locally assigned as the Hafir Mbr (Romein 1979).

The shift from marl-rich to chalk-rich sediments and the coeval appearance of cherts marks the transition from the Taqiye Fm to the Mor Fm within NP11 (~296 mbs). The Mor Fm (Fig. 4b) spans roughly 50 m and the contact with overlying Nizzana Fm lies at ~220 m, within NP13. The Nizzana Fm (Fig. 4c) is characterized in the studied section by a more yellowish color, reduced occurrence of chert and higher and more homogenous $CaCO_3$ and MS values. The boundary between the Nizzana and Horsha Fms is difficult to determine because of the lacking biostratigraphic datums above 225 mbs, but due to the absence of chert and homogenous light cream color (Fig. 4d) above ~130 mbs, the transition is tentatively placed at that depth.

5.2. Stable carbon isotope stratigraphy

Stable carbon isotope records of bulk sediment dominated by $CaCO_3$ and from isolated components (i. e. planktonic and benthic foraminifera) can be correlated at high temporal resolution across the Early Paleogene (e. g., Cramer et al. 2003, Zachos et al. 2008, Lauretano et al. 2016). As highlighted in several works (Dickens 2003, Sexton et al. 2011, Kirtland Turner et al. 2014), the reason for this lies in the rapid cycling of carbon between various Earth surface reservoirs and a highly dynamic global carbon cycle during this time. Starting with the biostratigraphy at Core RH-323, the bulk carbonate $\delta^{13}C$ record at this location was correlated to the high-resolution benthic foraminifera $\delta^{13}C$ records of Ocean Drilling Program (ODP) Sites 1262 and 1263 from Walvis Ridge in the southeast Atlantic Ocean (Littler et al. 2014, Lauretano et al. 2015, Lauretano et al. 2018) and 1209 from Shatsky Rise in the Pacific Ocean (Westerhold et al. 2011, Westerhold et al. 2018). This is best realized through six horizons (tie-points) in Core RH-323 (Table 1, Fig. 7).

Table 1. Carbon isotope stratigraphic tie-points. Ages are determined by correlation to benthic foraminifer isotope records of ODP 1262, ODP 1263.

#	Depth (mbs)	Age (Ma)	Carbon isotope tie-point
6	119.50	46.39	long-term low (C21n.H3)
5	167.70	48.73	long-term high (between C22n.H5 and C21r.H1)
4	226.45	51.26	Positive shift (C23n.2nH2; O)
3	250.05	52.86	ETM-3 (C24n.1nH1; K)
2	309.00	55.90	PETM
1	331.50	58.07	PCIM

The lowest tie-point at 331.5 mbs corresponds to the highest $\delta^{13}C$ value in global curves and represents the peak of the PCIM. Two negative $\delta^{13}C$ excursions close to the NP9–NP10 boundary may represent transient carbon isotope excursions, including the PETM: the anomalously low $\delta^{13}C$ value at 309 mbs and a more subtle negative excursion at 300 mbs. There are no significant analytical or lithological anomalies regarding these samples. The smaller $\delta^{13}C$ excursion at 300 mbs is closer to the LO of *T. bramlettei* that is used to pinpoint the NP9–NP10 boundary, and could therefore be the PETM. However, this bioevent has been regarded unreliable, because of ambiguous taxonomies (Agnini et al. 2014) and large offsets between calibrations of different studies, caused by either dissolution or diachroneity (e. g., Agnini et al. 2007). Furthermore, the $\delta^{13}C$ excursion at 300 mbs does not coincide with a significant spike in the $\delta^{18}O$ record, which is expected for the PETM. In contrast, the magnitude of both the $\delta^{13}C$ and $\delta^{18}O$ excursions at 309 mbs closely match that of the PETM at the neighboring Ben Gurion site (Schmitz et al. 1997). Although our sampling resolution varies across the record, it averages ~130 kyrs in the upper Paleocene and lower Eocene. Since the interval of sustained low values in the CIE of the PETM has a duration of ~170

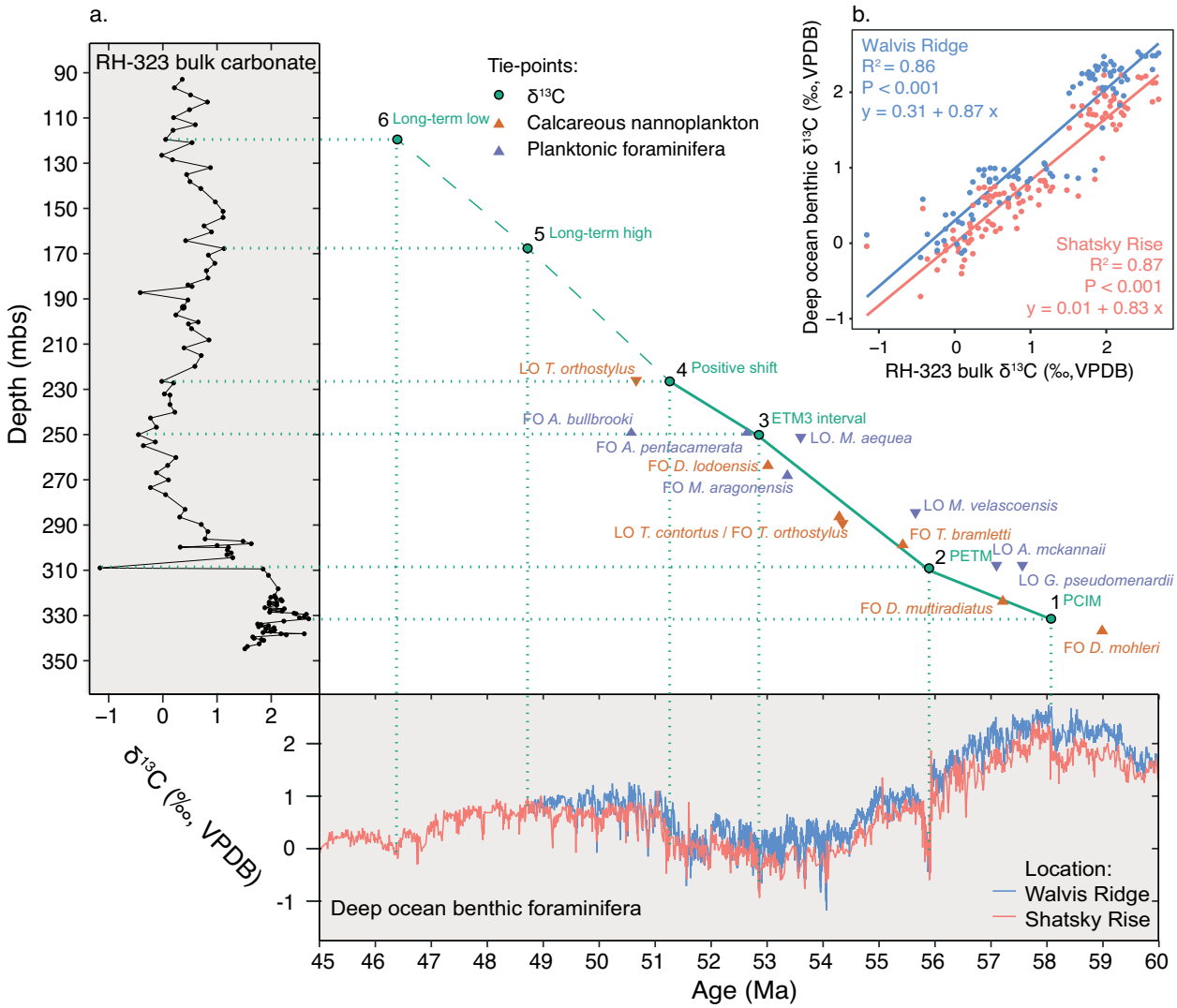

Fig. 7. Carbon isotope stratigraphic correlation between bulk carbonate from RH-323 and benthic isotope records from Walvis Ridge (Atlantic, Sites 1262 and 1263) and Shatsky Rise (Pacific, Site 1209). a) $\delta^{13}C$ record of RH-323 bulk carbonate (left) and deep ocean benthic foraminifera (bottom). The middle graph shows the age-depth model resulting from the carbon isotope correlation (green) together with the calcareous nannoplankton (orange) and planktonic foraminifer (purple) biostratigraphic datums. The dashed green line connects the two low-confidence tie-points in the upper part of the core. Benthic foraminifera isotope data is from McCarren et al. (2008), Stap et al. (2010), Westerhold et al. (2011, 2018), Littler et al. (2014), Lauretano et al. (2015, 2016). b) Right-top panel shows the linear regression analysis between RH-323 bulk carbonate $\delta^{13}C$ and open ocean benthic foraminifer $\delta^{13}C$ from Walvis ridge (Blue; $R^2 = 0.86$; $P < 0.001$; $y = 0.31 + 0.87$ x; n = 92) and Shatsky Rise (Red; $R^2 = 0.87$; $P < 0.001$; $y = 0.01 + 0.83$ x; n = 116) based on this carbon isotope stratigraphic correlation (see Discussion 5.2).

kyr (Zeebe and Lourens 2019), we might expect it to be represented by one sample in our record. Although follow-up work is desirable for full confirmation, we correlate the interval at 309 mbs to the PETM.

The long-term $\delta^{13}C$ low between ~270 and 180 mbs tracks the long-term minimum in other $\delta^{13}C$ records that spanned between ~54 and 51 Ma. We correlate the lowest $\delta^{13}C$ value at 250 mbs depth to ETM-3 (or K/X event), another brief interval characterized by low $\delta^{13}C$ values. A fourth tie-point can be placed in the middle of the ~0.6‰ positive $\delta^{13}C$ shift between ~226 and 220 mbs, as this corresponds to the step at ~51 Ma displayed in other $\delta^{13}C$ records. Due to the lack of clear biostratigraphic constraints above 225 mbs, it is difficult to confidently assign tie-points in the top half of the studied core section. We speculate that the ob-

served long-term high in $\delta^{13}C$ between 220 and 130 mbs and the overlying relatively low $\delta^{13}C$ values above 130 mbs correlate to similar trends in other stable isotope records, which occurred from approximately 51 to 47 Ma, and after 47 Ma, respectively. Two additional tie-points are drawn with this interpretation: the $\delta^{13}C$ high at 167.7 mbs is assigned an age of 48.7 Ma and the negative $\delta^{13}C$ values centered at 119.5 mbs an age of 46.4 Ma.

Clearly, the choice of tie points linking to well-dated $\delta^{13}C$ records elsewhere affects the age model for Core RH-323, which could improve with future analyses of more closely spaced samples. Nonetheless, we can test this stratigraphic correlation by a linear regression analysis between the RH-323 bulk carbonate $\delta^{13}C$ data (placed upon the new, carbon stratigraphic age model) and the benthic $\delta^{13}C$ records from Walvis Ridge and Shatsky Rise. Prior to this, the benthic $\delta^{13}C$ values were interpolated to the RH-323 dataset to allow direct comparison, and averaged over 50-ky to exclude high frequency variability. The resulting analysis (Fig. 7b) indicates remarkably high correlation coefficients for both the Atlantic ($R^2 = 0.86$) and Pacific Oceans ($R^2 = 0.87$) and slopes close to one (0.87 and 0.83, respectively). We therefore consider the major trend and features in our record to robustly represent changes in the $\delta^{13}C$ of the global exogenic carbon pool.

5.3. Absolute values of bulk carbonate carbon isotopes

Typically, for calcareous marine sediment deposited well away from the coast, bulk carbonate isotopes principally derive from calcareous nannofossils which inhabit the surface mixed layer (Stoll 2005, Reghellin et al. 2015, Bhattacharya et al. 2021). Remarkably, however, the bulk $\delta^{13}C$ record of Hole RH-323 is in very close agreement with the benthic records, not only in trends (see Discussion 5.2) but also in absolute values. This is evident from the two regression lines (Fig. 7b), which display intercepts that are close to zero (0.31 and 0.01, respectively for the Atlantic and Pacific Oceans). The difference between the two intercepts represents the ~0.3‰ offset between the Pacific and Atlantic oceanic basins (e. g., Westerhold et al. 2018), and indicates that RH-323 bulk values are closest to Pacific benthic $\delta^{13}C$ values. Such a close correspondence with absolute benthic $\delta^{13}C$ values is not principally expected from a bulk carbonate $\delta^{13}C$ signal, as the surface mixed layer dissolved inorganic carbon (DIC) is commonly 1–2‰ enriched in $\delta^{13}C$ compared to deep water (Hilting et al. 2008). Comparing several sites with moderately to very detailed bulk carbonate $\delta^{13}C$ records across the late Paleocene through middle Eocene interval confirms that, for most of this time, the record at RH-323 displays a significant negative offset (~1–2‰) relative to records from other sites (Fig. 8). The offset becomes much smaller, however, during the latest Paleocene and earliest Eocene (56.5–55 Ma), and during the latest early Eocene (47–49 Ma).

Relative to other $\delta^{13}C$ records, the negative offset as well as the late Paleocene convergence also manifests at the Ben Gurion outcrop section in the Zin Valley, approximately 30 km south of RH-323 (Charisi and Schmitz 1998). Interestingly, these features also appear in benthic foraminifer $\delta^{13}C$ records from this location, and while limited to a single datapoint, the magnitude of the CIE at the PETM (~3‰) agrees with that found in bulk carbonate at other sites from Israel and Egypt (Schmitz et al. 1996, Charisi and Schmitz 1998). Clearly, the intriguing issue is not confined to the samples of Core RH-323.

Secondary precipitation or recrystallization of carbonate, either on the seafloor or especially after burial provides one potential explanation for the observed offset in bulk carbonate $\delta^{13}C$ relative to that at most other locations (Schrag et al. 1995, Frank et al. 1999, Staudigel and Swart 2019). However, this is especially true for oxygen isotope ratios, stable carbon isotope ratios are much less affected (Banner and Hanson 1990, Slotnick et al. 2015). Indeed, the correlative trends in $\delta^{13}C$ (Figs. 7, 8) almost necessarily advocate against a significant burial-related diagenetic overprint in our dataset. Moreover, the majority of the studied sediments have not been lithified to limestone and still consist of chalk, likely due to shallow burial depth. Further, no clear relationship between $\delta^{13}C$ values, $\delta^{18}O$ values and wt%$CaCO_3$ exists in our samples (Fig. 6g–h), which suggests that no significant precipitation or recrystallization of carbonate has occurred (Frank et al. 1999, Slotnick et al. 2015).

In general, the $\delta^{13}C$ composition of marine calcareous sediment depends on three factors (Sluijs and Dickens 2012): a) the relative abundance of various carbonate components, b) the carbon isotope fractionations between carbonate and surrounding DIC for the individual components, and c) the $\delta^{13}C$ of the DIC. In some cases, carbonate components other than calcareous nannofossils, with different fractionation, may become significant. For instance, in marginal settings, the bulk $\delta^{13}C$ signal can contain large amounts of material transported from adjacent neritic

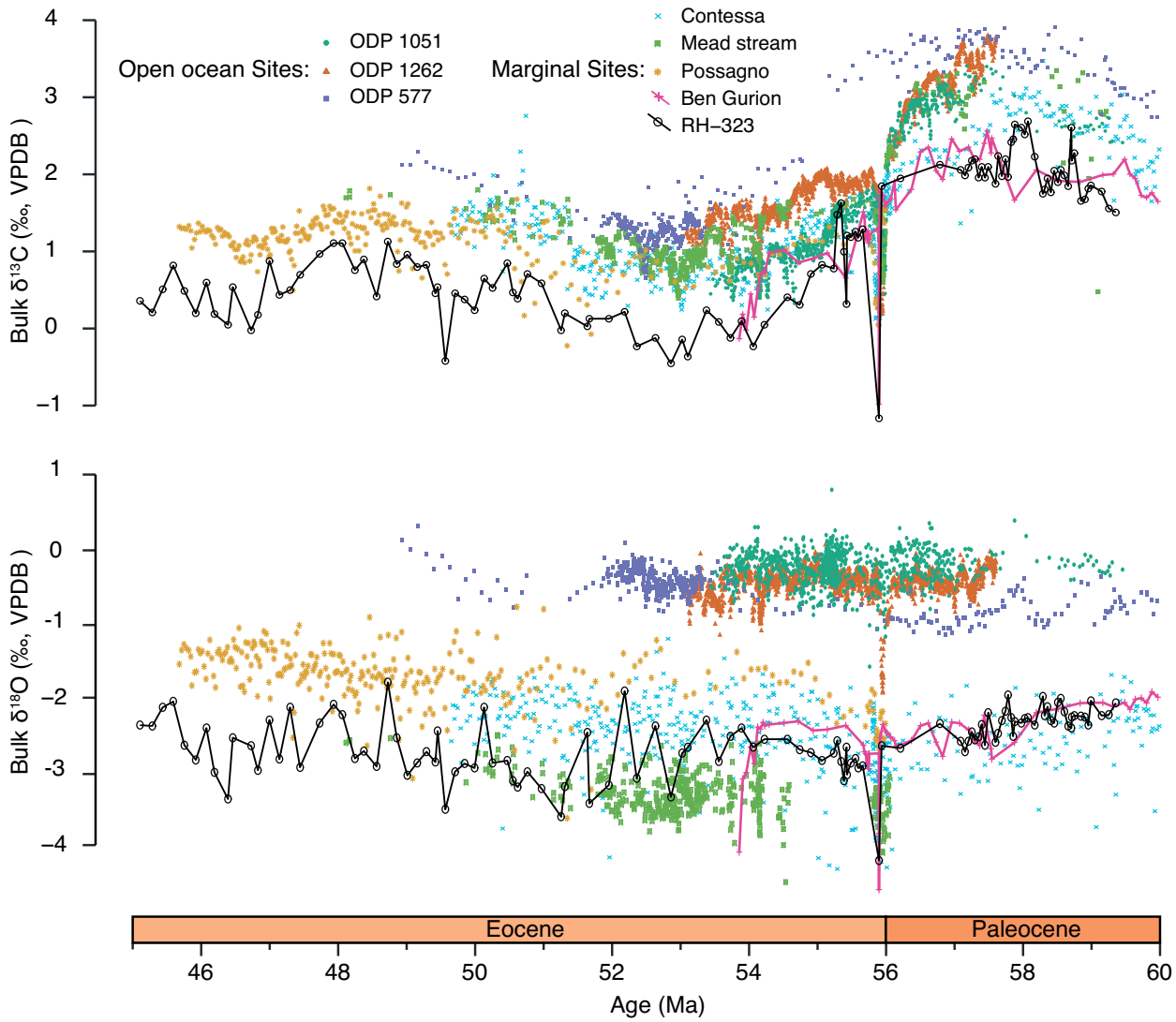

Fig. 8. Comparison of bulk carbonate carbon and oxygen isotope records from RH-323 (this study) to bulk isotope records from other locations. Data is retrieved from Hollis et al. (2005), Nicolo et al. (2007, 2010), Slotnick et al. 2012 (Mead Stream, New Zealand), Cramer et al. (2003), Shackleton et al. (1985) (DSDP Site 577, Pacific Ocean), Cramer et al. (2003 (ODP Site 1051, Blake Nose, Western North Atlantic), Lourens et al. (2005), Zachos et al. (2010) (ODP 1262, Walvis Ridge, Southeast Atlantic), Luciani et al. (2016) (Possagno, Northern Italy), Coccioni et al. (2012) (Contessa, Central Italy) and Charisi and Schmitz (1998) (Ben Gurion, Israel).

environments (Swart 2008, Swart 2019). Another case arises with high contents of planktonic or benthic foraminifera, both that can have significantly different $\delta^{13}C$ compositions than calcareous nannoplankton (Reghellin et al. 2015, Bhattacharya et al. 2021). In addition, high primary production might regionally lead to a rise in surface ocean $\delta^{13}C$ of DIC as ^{12}C is preferentially fixed, but that does not explain our low values. Without further sample analysis and determining the abundances and $\delta^{13}C$ compositions of various carbonate components, we cannot fully argue that the offset represents a major difference in the $\delta^{13}C$ of the DIC in southern Israel relative to other locations.

Two general explanations for regionally lowered surface $\delta^{13}C$ would be warmer waters or more brackish waters than most marine locations. This is because the $\delta^{13}C$ of surface water DIC depends on temperature through equilibrium fractionation between the surface ocean and atmospheric CO_2 (Mook et al. 1974) and a significant correlation occurs between the $\delta^{13}C$ of DIC and salinity through the effect of conservative mixing of ^{13}C-depleted river water and seawater (Fry 2002). In

either case, the $\delta^{18}O$ of bulk carbonate should also be lower relative to other locations.

5.4. Absolute values of bulk carbonate oxygen isotope ratios

Bulk carbonate $\delta^{18}O$ values are ~2‰ lower than those from most open ocean sites, but slightly higher than those recorded at Mead Stream (Slotnick et al. 2012, Fig. 8). While this may support the interpretation of the above mentioned $\delta^{13}C$ offset, the differences may also reflect alteration of original signals. Paleogene carbonate in key open ocean drill sites has remained as "ooze", although in some cases it has converted to chalk. In the latter case, which generally occurs at fairly shallow burial depths, O-isotope exchange with pore water during carbonate reprecipitation occurs at temperatures lower than those in surface waters. This tends to increase the $\delta^{18}O$ of carbonate components (e. g., Schrag et al. 1995). By contrast, the lithology at Mead Stream is limestone, which may have recrystallized at greater burial depth at temperatures higher than surface waters. Moreover, the uplifted section may have been affected further by exchange with meteoric water (Slotnick et al. 2012). Both processes tend to decrease the $\delta^{18}O$ of carbonate components.

Disregarding the above complexities, and assuming that bulk carbonate is comprised mostly of nannofossils, a back-of-the-envelope calculation of surface water temperatures can be made using well-known equations that relate the $\delta^{18}O$ of calcite and water to temperature (Kim and O'Neil 1997, Bemis et al. 1998). With the further assumptions of a 1‰ offset for calcareous nannoplankton vital effects (Reghellin et al. 2015), and a seawater $\delta^{18}O$ value of –0.15‰ (given a continental ice-free world) (Zachos et al. 1994), estimated temperatures lie between ~29 and 42 °C. These values fall within expectations for late Paleocene through early Eocene low latitude surface waters according to estimates based on different proxies (Giusberti et al. 2014, Cramwinckel et al. 2018, Evans et al. 2018, Barnet et al. 2020). Note that this temperature estimate is here solely used to test if $\delta^{18}O$ values are within expected range and should not be considered as an accurate sea surface temperature reconstruction. Naturally, it is expected that planktonic foraminifer oxygen isotope data should yield more accurate reconstructions of surface water temperatures, because they allow for species-specific corrections of vital effects (e. g., Bemis et al. 1998) and scanning electron microscopic assessment of diagenesis (e. g., Sexton et al. 2006).

5.5. Lithostratigraphic variance

With detailed descriptions of Paleocene-Eocene outcrop sections and drill cores from around the world, an interesting observation has emerged: at numerous locations, the sediment composition varies in concert with changes in global environmental conditions. This is obvious for the PETM, where a change in lithology marks the event almost everywhere, although the physical expression and cause for the sedimentary change differs. For example, it is a clay rich horizon in many deep-sea sections, presumably because of carbonate dissolution (Zachos et al. 2005), but a conglomerate in several Spanish sections, presumably because of enhanced seasonal rainfall (Pujalte et al. 2015, Chen et al. 2018). Interestingly, at least in sections from Clarence Valley (New Zealand), lithological changes also mark other intervals of global change, including multiple early Eocene hyperthermals, the PCIM and the EECO (Hollis et al. 2005, Nicolo et al. 2007, Slotnick et al. 2012, Slotnick et al. 2015).

For the generally marl dominated Taqiye Fm, the highest $\delta^{13}C$ values mark the PCIM and span the calcareous Hafir Mbr (Fig. 9). The alignment of the PCIM with a chalk-rich unit may be a consistent feature for regional lithostratigraphy, with lateral equivalents (e. g., Tarawan Fm in Egypt) extending across the Southern Tethys margin (e. g., Schmitz et al. 1997).

The CIE and benthic extinction event related to the PETM is regionally observed within a calcarenitic layer (Charisi and Schmitz 1995, Charisi and Schmitz 1998, Schmitz et al. 1997, Bolle et al. 2000, Speijer and Wagner 2002). The CIE at 309 mbs within Core RH-323, which correlates to the PETM, is coeval with a drop in the MS data (to ~2.5×10^{-8} χ) and a thin whitish layer, suggesting the presence of a calcareous layer as well.

The lithological transition from the marl dominated Taqiye Fm to the chalk dominated Mor Fm is a depositional shift also observed to the west of the area (Egypt) as the transition from the Esna to the Thebes Fms (El-Azabi and Farouk 2011) and is contemporaneous with the onset of the EECO (Fig. 9). This transition aligns with the appearance of cherts, which are abundant in both the Mor and Nizzana Fms (Fig. 5) and characterize many globally distributed

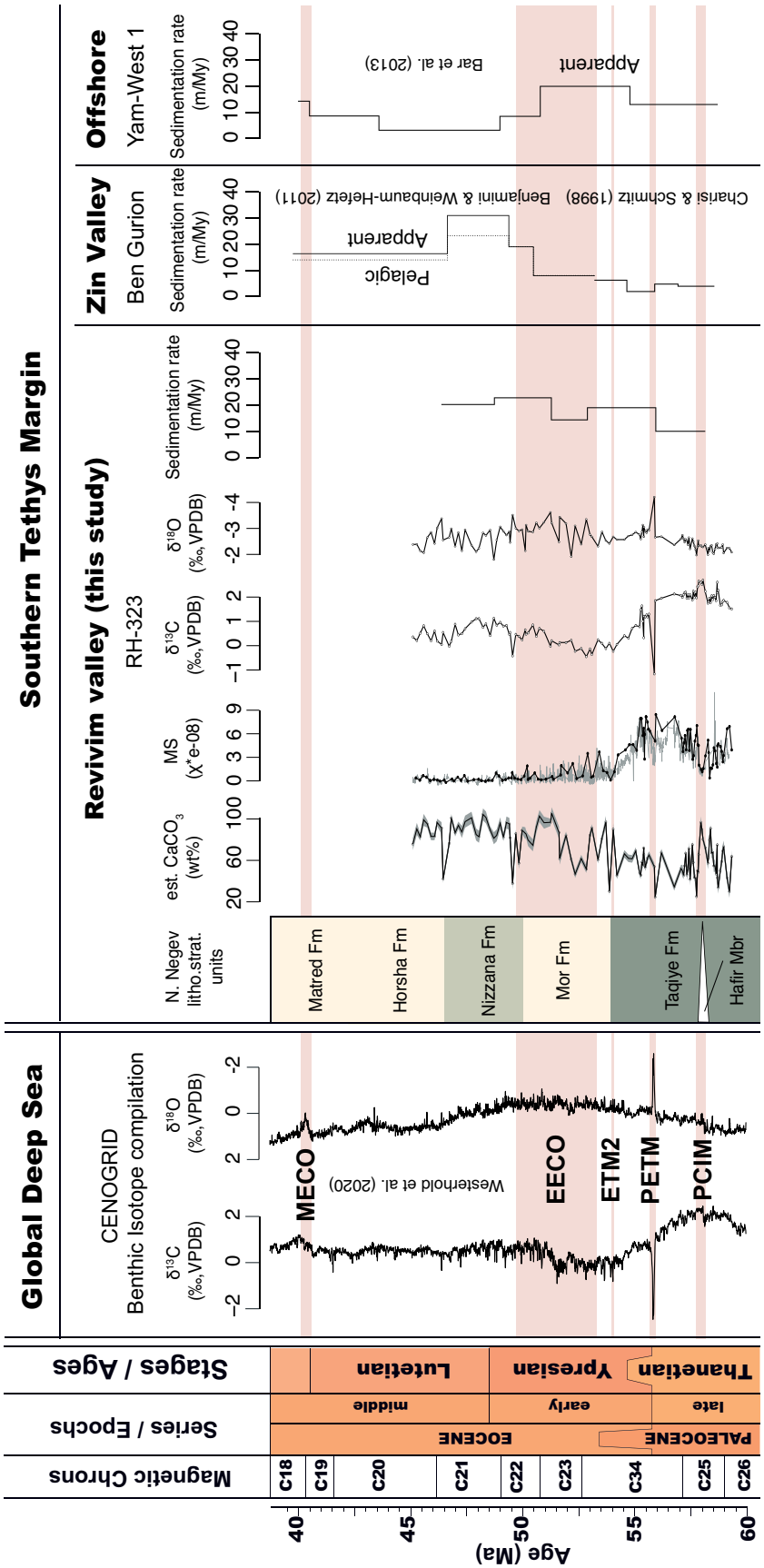

Fig. 9. Comparison of current study's results with sedimentation rate patterns from neighboring locations and deep ocean benthic foraminifer isotope variations. Ages are according to GPTS 2012 (Gradstein et al. 2012), with astronomically calibrated Ypresian by Westerhold et al. (2017). Global deep sea benthic isotope ratios are retrieved from the CENOGRID compilation of Westerhold et al. (2020). The sedimentation rates from the Ben Gurion section are based on biostratigraphy from Charisi and Schmitz (1998) and Weinbaum-Hefetz and Benjamini (2011), where dotted sedimentation rates are subtracted for identified mass-transported beds. Sedimentation rates from the offshore section are based on biostratigraphic age model of the Yam-West 1 borehole by Bar et al. (2013). Results from current research of Borehole RH-323 include: wt%CaCO3, as estimated by mass-spec intensity with uncertainty (1σ) represented by grey band, discrete (black) and continuous (grey; from Opuwari et al. (2021)) bulk magnetic susceptibility, bulk carbon and oxygen isotopes and sedimentation rate calculated by carbon isotope chemostratigraphic age model.

Lower Eocene sections (Muttoni and Kent 2007). Interestingly, in the New Zealand marginal sections, the onset of the EECO corresponds to the transition from limestones to marls, which has been interpreted as a warming-induced intensification of the hydrological cycle, and a conspicuous absence of chert (Hollis et al. 2005, Slotnick et al. 2012, Slotnick et al. 2015). If, like on the New Zealand margins, lithological changes associated with the EECO on the Southern Tethys margin were similarly linked to variations in global hydrological cycling, this would suggest pronounced heterogeneity in hydrological response along continental margins. This heterogenous response conforms with a general first-order view that, under globally rising temperatures, vapor transport increases from moisture convergence zones to moisture divergence zones (Held and Soden 2006). This simplified 'dry-gets-drier, wet-gets-wetter' response broadly fits previous model and proxy reconstructions of Paleogene warming events (Carmichael et al. 2017). However, while, the hydrological model output of Carmichael et al. (2017) for the PETM matches increased precipitation at the New Zealand margins during early Paleogene warming, it does not indicate significant hydrologic changes in the Southern Tethyan region. Alternatively, although increasingly dry conditions are supported by clay mineral analysis (Bolle et al. 2000), early Eocene variations in terrestrial input on the southern Tethys margin could in part be forced by changes in relative sea level rise, and variations between river discharge and shelf width.

5.6. Spatial variability of sedimentation rates

Sedimentation rates can be calculated using the carbon isotopic age model of Core RH-323 (Fig. 9). These rates generally rise from ~10 m My^{-1} in the Taqiye Fm to >20 m My^{-1} in the Nizzana Fm. A somewhat similar trend is recorded in the neighboring Zin Valley, where rates increase from 7.5 m My^{-1} in the Mor Fm to 23.6 m My^{-1} in the Nizzana Fm (Charisi and Schmitz 1998, Weinbaum-Hefetz and Benjamini 2011). Because of apparent mass transport beds in the Nizzana Fm, Weinbaum-Hefetz and Benjamini (2011) corrected sedimentation rates by subtracting them. Although the observed increase may be caused in part by unidentified mass transport beds, an opposing depositional trend is recorded offshore in the Levant Basin (Yam-West 1 well) (Bar et al. 2013), with high sedimentation rates (~20 m My^{-1}) in the early Eocene and a striking decline in sedimentation rates toward only ~5 m My^{-1} in the middle Eocene. Clearly, this discrepancy cannot be explained by mass transport deposits on the continental slope. An alternative mechanism could be related to a spatial shift in productivity, either related to localized upwelling or nutrient distribution, shifting from offshore above the Levant Basin during the early Eocene toward the position of the present-day northern Negev in the middle Eocene. Consistent with this hypothesis, calcareous nannofossil assemblages in the Zin Valley do indicate a transition from oligotrophic and stratified conditions during the early Eocene to high productivity at the late-early Eocene (Weinbaum-Hefetz and Benjamini 2011).

6. Conclusions and future research

Following early work by others on southern Tethys margin sections (e. g., Charisi and Schmitz 1995, Charisi and Schmitz 1998, Schmitz et al. 1997, Bolle et al. 2000, Speijer and Wagner 2002), we generated records of lithology, stable oxygen and carbon isotopes, MS and wt%$CaCO_3$ using samples from Core RH-323. The overall aim was to establish the suitability of lower Paleogene sections in southern Israel for regional paleoclimate and paleo-environment reconstructions. These sections may be especially important because they have not been lithified to limestone. Our analyses show that bulk carbonate carbon and oxygen isotope analyses give interpretable signals. The isotope results, combined with available biostratigraphic work, indicate a virtually continuous late Paleocene to middle Eocene section, which can be correlated to deep ocean records. A 1–2 ‰ negative $\delta^{13}C$ offset relative to a global set of bulk carbonate records is observed over the majority of the interval. Sea surface temperatures calculated from oxygen isotopes yield values within the expected range, which may indicate the preservation of a primary oxygen isotopic composition of biogenic calcite. Lithological variations in the studied section, which include a transition from the marl rich Taqiye Fm to the chalky Mor Fm, and punctuation of the Taqiye marls by a carbonate interval appear to be manifestations of contemporaneous carbon cycle and climate variations. We conclude that the complete nature of the studied deposits and quality of the sampled material is rare for a marginal section and deserves priority in higher resolution studies in the near future. We anticipate such high-resolution data from sites in the Northern

Negev will ultimately give valuable insights into the reaction of local productivity, hydrology or relative sea-level to global climate changes in the early Paleogene.

Acknowledgements. We thank the European Research Council for Consolidator Grant 771497 awarded to AS, funded under Horizon 2020 program, and Arnold van Dijk and Maxim Krasnoperov (Utrecht University) for technical support. GD and JF received support for travel and fieldwork through a Netherlands Earth System Science Centre (NESSC) Sabbatical Grant.

References

Adar, E. M., Nativ, R., Siman-Tov, R., Eshet, Y., 1999. The deep corehole (RH-323) in Ramat Hovav. Final Report submitted to the Israeli Water Authority. Geological Survey Report GSI/6/99.

Agnini, C., Fornaciari, E., Raffi, I., Catanzariti, R., Pälike, H., Backman, J., Rio, D., 2014. Biozonation and biochronology of Paleogene calcareous nannofossils from low and middle latitudes. Newsletters on Stratigraphy 47, 131–181.

Agnini, C., Fornaciari, E., Raffi, I., Rio, D., Röhl, U., Westerhold, T., 2007. High-resolution nannofossil biochronology of middle Paleocene to early Eocene at ODP Site 1262: Implications for calcareous nannoplankton evolution. Marine Micropaleontology 64, 215–248.

Agnini, C., Macri, P., Backman, J., Brinkhuis, H., Fornaciari, E., Giusberti, L., Luciani, V., Rio, D., Sluijs, A., Speranza, F., 2009. An early Eocene carbon cycle perturbation at ~52.5 Ma in the Southern Alps: Chronology and biotic response. Paleoceanography 24, PA2209.

Agnini, C., Muttoni, G., Kent, D. V., Rio, D., 2006. Eocene biostratigraphy and magnetic stratigraphy from Possagno, Italy: The calcareous nannofossil response to climate variability. Earth and Planetary Science Letters 241, 815–830.

Banner, J. L., Hanson, G. N., 1990. Calculation of simultaneous isotopic and trace element variations during water-rock interaction with applications to carbonate diagenesis. Geochimica et Cosmochimica Acta 54, 3123–3137.

Bar, O., Gvirtzman, Z., Feinstein, S., Zilberman, E., 2013. Accelerated subsidence and sedimentation in the Levant basin during the Late Tertiary and concurrent uplift of the Arabian platform: Tectonic versus counteracting sedimentary loading effects. Tectonics 32, 334–350.

Barnet, J., Harper, D. T., LeVay, L. J., Edgar, K. M., Henehan, M. J., Babila, T. L., Ullmann, C. V., Leng, M. J., Kroon, D., Zachos, J. C., Littler, K., 2020. The Coupled Evolution of Temperature and Carbonate Chemistry during the Paleocene – Eocene; New Orbital-Resolution Trace Metal Records from the Low-Latitude Indian Ocean. Earth and Planetary Science Letters 545, 116414.

Bartov, J., Eyal, Y., Garfunkel, Z., Steinitz, G., 1972. Late Cretaceous and Tertiary Stratigraphy and Paleogeography of Southern Israel. Israel Journal of Earth Sciences 21, 69–97.

Bemis, B. E., Spero, H. J., Bijma, J., Lea, D. W., 1998. Reevaluation of the oxygen isotopic composition of planktonic foraminifera: Experimental results and revised paleotemperature equations. Paleoceanography 13, 150–160.

Benjamini, C., 1980a. Planktonic Foraminiferal Biostratigraphy of the 'Avedat Group (Eocene) in the Northern Negev, Israel. Journal of Paleontology 54, 325–358.

Benjamini, C., 1980b. Stratigraphy and Foraminifera of the Qezi'ot and Har'Aqrav Formations (Latest Middle to Late Eocene) of the Western Negev, Israel. Israel Journal of Earth Sciences 29, 227–244.

Bentor, Y. K., Vroman, A., 1960. The geological map of Israel, 1:100,000. Sheet 16: Mount Sdom. Geological Survey, Israel, Jerusalem.

Berggren, W. A., Kent, D. V., Swisher, C. C., Aubry, M. P., 1995. A revised Cenozoic geochronology and chronostratigraphy. Geochronology, Time Scales and Global Stratigraphic Correlation 54, 129–212.

Bhattacharya, J., Yeung, L. Y. Y., Cong, L., Dickens, G. R., Sun, T., 2021. Size-Fraction-Specific Stable Isotope Variations as a Framework for Interpreting Early Eocene Bulk Sediment Carbon Isotope Records. Paleoceanography and Paleoclimatology 36, e2020PA004132.

Bijl, P. K., Pross, J., Warnaar, J., Stickley, C. E., Huber, M., Guerstein, R., Houben, A. J. P., Sluijs, A., Visscher, H., Brinkhuis, H., 2011. nvironmental forcings of Paleogene Southern Ocean dinoflagellate biogeography. Paleoceanography 26, PA1202.

Bijl, P. K., Schouten, S., Sluijs, A., Reichart, G. J., Zachos, J., Brinkhuis, H., 2009. Early palaeogene temperature evolution of the southwest Pacific Ocean. Nature 461, 776–779.

Blanckenhorn, M., 1925. Die Seeigelfauna der Kreide Palästinas. Palaeontographica (1846-1933) 67, 83–114.

Bolle, M. P., Pardo, A., Adatte, T., Tantawy, A. A., Hinrichs, K. U., Von Salis, K., Burns, S., 2000. Climatic evolution on the southern and northern margins of the Tethys from the Paleocene to the early Eocene. Journal of the Geological Society, London 157, 929–941.

Carmichael, M. J., Inglis, G. N., Badger, M. P. S., Naafs, B. D. A., Behrooz, L., Remmelzwaal, S., Monteiro, F. M., Rohrssen, M., Farnsworth, A., Buss, H. L., Dickson, A. J., Valdes, P., Lunt, D. J., Pancost, R. D., 2017. Hydrological and associated biogeochemical consequences of rapid global warming during the Paleocene-Eocene Thermal Maximum. Global and Planetary Change 157, 114–138.

Charisi, S. D., Schmitz, B., 1995. Paleocene at Gebel Aweina, eastern Tethyan region. Palaeogeography, Palaeoclimatology, Palaeoecology 116, 103–129.

Charisi, S. D., Schmitz, B., 1998. Paleocene to early eocene paleoceanography of the middle east: The $\delta^{13}C$ and $\delta^{18}O$

isotopes from foraminiferal calcite. Paleoceanography 13, 106–118.

Chen, C., Guerit, L., Foreman, B. Z., Hassenruck-Gudipati, H. J., Adatte, T., Honegger, L., Perret, M., Sluijs, A., Castelltort, S., 2018. Estimating regional flood discharge during Palaeocene-Eocene global warming. Scientific Reports 8, 13391.

Coccioni, R., Bancalà, G., Catanzarit, R., Fornaciari, E., Frontalini, F., Giusberti, L., Jovane, L., Luciani, V., Savian, J., Sprovieri, M., 2012. An integrated stratigraphic record of the Palaeocene-lower Eocene at Gubbio (Italy): New insights into the early Palaeogene hyperthermals and carbon isotope excursions. Terra Nova 24, 380–386.

Cramer, B. S., Wright, J. D., Kent, D. V., Aubry, M. P., 2003. Orbital climate forcing of δ13C excursions in the late Paleocene-early Eocene (chrons C24n-C25n). Paleoceanography 18, 1097.

Cramwinckel, M. J., Huber, M., Kocken, I. J., Agnini, C., Bijl, P. K., Bohaty, S. M., Frieling, J., Goldner, A., Hilgen, F. J., Kip, E. L., Peterse, F., Van Der Ploeg, R., Röhl, U., Schouten, S., Sluijs, A., 2018. Synchronous tropical and polar temperature evolution in the Eocene letter. Nature 559, 382–386.

Crouch, E. M., Shepherd, C. L., Morgans, H. E. G., Naafs, B. D. A., Dallanave, E., Phillips, A., Hollis, C. J., Pancost, R. D., 2020. Climatic and environmental changes across the early Eocene climatic optimum at mid-Waipara River, Canterbury Basin, New Zealand. Earth-Science Reviews 200, 102961.

Dickens, G. R., 2003. Rethinking the global carbon cycle with a large, dynamic and microbially mediated gas hydrate capacitor. Earth and Planetary Science Letters 213, 169–183.

El-Azabi, M. H., Farouk, S., 2011. High-resolution sequence stratigraphy of the Maastrichtian-Ypresian succession along the eastern scarp face of Kharga Oasis, southern Western Desert, Egypt. Sedimentology 58, 579–617.

Eshet, Y., Siman-Tov, R., 2000. Subsurface biostratigraphy of the Paleocene in the Ramat Hovav area. Geological Society Israel Current Research 12, 193–196.

Evans, D., Sagoo, N., Renema, W., Cotton, L. J., Müller, W., Todd, J. A., Saraswati, P. K., Stassen, P., Ziegler, M., Pearson, P. N., Valdes, P., Affek, H. P., 2018. Eocene greenhouse climate revealed by coupled clumped isotope-Mg/Ca thermometry. Proceedings of the National Academy of Sciences of the United States of America 115, 1174–1179.

Frank, T. D., Arthur, M. A., Dean, W. E., 1999. Diagenesis of lower Cretaceous pelagic carbonates, North Atlantic: Paleoceanographic signals obscured. Journal of Foraminiferal Research 29, 340–351.

Fry, B., 2002. Conservative mixing of stable isotopes across estuarine salinity gradients: A conceptual framework for monitoring watershed influences on downstream fisheries production. Estuaries 25, 264–271.

Giusberti, L., Bannikov, A., Boscolo Galazzo, F., Fornaciari, E., Frieling, J., Luciani, V., Papazzoni, C. A., Roghi, G., Schouten, S., Sluijs, A., Bosellini, F. R., Zorzin, R., 2014. A new fossil-lagerstätte from the lower eocene of lessini mountains (northern Italy): A multidisciplinary approach. Palaeogeography, Palaeoclimatology, Palaeoecology 403, 1–15.

Gradstein, F. M., Ogg, J. G., Schmitz, M. D., Ogg, C. M., 2012. The Geological Time Scale 2012, Elsevier, Amsterdam.

Gvirtzman, Z., 2004. Chronostratigraphic table and subsidence curves of southern Israel. Israel Journal of Earth Sciences 53, 47–61.

Gvirtzman, Z., Steinberg, J., Bar, O., Buchbinder, B., Zilberman, E., Siman-Tov, R., Calvo, R., Grossowicz, L., Almogi-Labin, A., Rosensaft, M., 2011. Retreating late tertiary shorelines in Israel: Implications for the exposure of north Arabia and levant during Neotethys closure. Lithosphere 3, 95–109.

Held, I. M., Soden, B. J., 2006. Robust responses of the hydrological cycle to global warming. Journal of Climate 19, 5686–5699.

Hilting, A. K., Kump, L. R., Bralower, T. J., 2018. ariations in the oceanic vertical carbon isotope gradient and their implications for the Paleocene-Eocene biological pump. Paleoceanography 23, PA3222.

Hollis, C. J., Dickens, G. R., Field, B. D., Jones, C. M., Percy Strong, C., 2005. The Paleocene-Eocene transition at Mead Stream, New Zealand: A southern Pacific record of early Cenozoic global change. Palaeogeography, Palaeoclimatology, Palaeoecology 215, 313–343.

Hollis, C. J., Dunkley Jones, T., Anagnostou, E., Bijl, P. K., Cramwinckel, M. J., Cui, Y., Dickens, G. R., Edgar, K. M., Eley, Y., Evans, D., Foster, G. L., Frieling, J., Inglis, G. N., Kennedy, E. M., Kozdon, R., Lauretano, V., Lear, C. H., Littler, K., Lourens, L. J. , …, Lunt, D. J., 2019. The DeepMIP contribution to PMIP4: Methodologies for selection, compilation and analysis of latest Paleocene and early Eocene climate proxy data, incorporating version 0.1 of the DeepMIP database. Geoscientific Model Development 12, 3149–3206.

Honigstein, A., Rosenfeld, A., Benjamini, C., 2002. Eocene ostracode faunas from the Negev, southern Israel: Taxonomy, stratigraphy and paleobiogeography. Micropaleontology 48, 365–389.

Hotinski, R. M., Toggweiler, J. R., 2003. Impact of a Tethyan circumglobal passage on ocean heat transport and "equable" climates. Paleoceanography 18, 1007.

Hunt, C. P., Moskowitz, B. M., Banerjee, S. K., 1995. Magnetic Properties of Rocks and Minerals. Rock Physics and Phase Relations: A Handbook of Physical Constants 3, 189–204.

John, C. M., Bohaty, S. M., Zachos, J., Sluijs, A., Gibbs, S., Brinkhuis, H., Bralower, T. J., 2008. North American continental margin records of the Paleocene-Eocene thermal maximum: Implications for global carbon and hydrological cycling. Paleoceanography 23, PA2217.

Kennett, P., Stott, D., 1991. Abrupt deep-sea warming, paleoceanographic changes and benthic extinctions at the end of the Palaeocene. Nature 353, 225–229.

Kim, S. T., O'Neil, J. R., 1997. Equilibrium and nonequilibrium oxygen isotope effects in synthetic carbonates. Geochimica et Cosmochimica Acta 61, 3461–3475.

Kirtland Turner, S., Sexton, P. F., Charles, C. D., Norris, R. D., 2014. Persistence of carbon release events through the peak of early Eocene global warmth. Nature Geoscience 7, 748–751.

Komar, N., Zeebe, R. E., Dickens, G. R., 2013. Understanding long-term carbon cycle trends: The late Paleocene through the early Eocene. Paleoceanography 28, 650–662.

Krenkel, E., 1924. Der Syrische Bogen. Zentralblad für Mineralogie, Geologie und Paläontology 9, 274–281.

Kump, L. R., Arthur, M. A., 1999. Interpreting carbon-isotope excursions: Carbonates and organic matter. Chemical Geology 161, 181–198.

Kurtz, A. C., Kump, L. R., Arthur, M. A., Zachos, J., Paytan, A., 2003. Early Cenozoic decoupling of the global carbon and sulfur cycles. Paleoceanography 18, 1090.

Lauretano, V., Hilgen, F. J., Zachos, J., Lourens, L. J., 2016. Astronomically tuned age model for the early Eocene carbon isotope events: A new high-resolution δ13C benthic record of ODP Site 1263 between ~49 and ~54 Ma. Newsletters on Stratigraphy 49, 383–400.

Lauretano, V., Littler, K., Polling, M., Zachos, J., Lourens, L. J., 2015. Frequency, magnitude and character of hyperthermal events at the onset of the Early Eocene Climatic Optimum. Climate of the Past 11, 1313–1324.

Lauretano, V., Zachos, J., Lourens, L. J., 2018. Orbitally Paced Carbon and Deep-Sea Temperature Changes at the Peak of the Early Eocene Climatic Optimum. Paleoceanography and Paleoclimatology 33, 1050–1065.

Littler, K., Röhl, U., Westerhold, T., Zachos, J., 2014. A high-resolution benthic stable-isotope record for the South Atlantic: Implications for orbital-scale changes in Late Paleocene-Early Eocene climate and carbon cycling. Earth and Planetary Science Letters 401, 18–30.

Liu, Q., Roberts, A. P., Larrasoaa, J. C., Banerjee, S. K., Guyodo, Y., Tauxe, L., Oldfield, F., 2012. Environmental magnetism: Principles and applications. Reviews of Geophysics 50, RG4002.

Lourens, L. J., Sluijs, A., Kroon, D., Zachos, J., Thomas, E., Röhl, U., Bowles, J., Raffi, I., 2005. Astronomical pacing of late Palaeocene to early Eocene global warming events. Nature 435, 1083–1087.

Luciani, V., Dickens, G. R., Backman, J., Fornaciari, E., Giusberti, L., Agnini, C., D'Onofrio, R., 2016. Major perturbations in the global carbon cycle and photosymbiont-bearing planktic foraminifera during the early Eocene. Climate of the Past 12, 981–1007.

Luciani, V., Giusberti, L., 2014. Reassessment of the early-middle Eocene planktic foraminiferal biomagnetochronology: New evidence from the tethyan possagno section (ne Italy) and western North Atlantic Ocean ODP Site 1051. Journal of Foraminiferal Research 44, 187–201.

McCarren, H., Thomas, E., Hasegawa, T., Röhl, U., Zachos, J., 2008. Depth dependency of the paleocene-eocene carbon isotope excursion: Paired benthic and terrestrial biomarker records (ocean drilling program leg 208, Walvis Ridge). Geochemistry, Geophysics, Geosystems 9, Q10008.

McInerney, F. A., Wing, S. L., 2011. The Paleocene-Eocene Thermal Maximum: A Perturbation of Carbon Cycle, Climate, and Biosphere with Implications for the Future. Annual Review of Earth and Planetary Sciences 39, 489–516.

Meilijson, A., Ashckenazi-Polivoda, S., Ron-Yankovich, L., Illner, P., Alsenz, H., Speijer, R. P., Almogi-Labin, A., Feinstein, S., Berner, Z., Püttmann, W., Abramovich, S., 2014. Chronostratigraphy of the Upper Cretaceous high productivity sequence of the southern Tethys, Israel. Cretaceous Research 50, 187–213.

Mook, W. G., Bommerson, J. C., Staverman, W. H., 1974. Carbon isotope fractionation between dissolved bicarbonate and gaseous carbon dioxide. Earth and Planetary Science Letters 22, 169–176.

Muttoni, G., Kent, D. V., 2007. Widespread formation of cherts during the early Eocene climate optimum. Palaeogeography, Palaeoclimatology, Palaeoecology 253, 348–362.

Nicolo, M. J., Dickens, G. R., Hollis, C. J., 2010. South Pacific intermediate water oxygen depletion at the onset of the Paleocene-Eocene thermal maximum as depicted in New Zealand margin sections. Paleoceanography 25, PA4210.

Nicolo, M. J., Dickens, G. R., Hollis, C. J., Zachos, J., 2007. Multiple early Eocene hyperthermals: Their sedimentary expression on the New Zealand continental margin and in the deep sea. Geology 35, 699–702.

Ogg, J. G., 2020. Geomagnetic Polarity Time Scale. In: Gradstein, F. M., Ogg, J. G., Schmitz, M. D., Ogg, G. M. (Eds.), Geologic Time Scale 2020, Elsevier, Amsterdam, 159–192.

Opuwari, M., Bialik, O. M., Taha, N., Waldmann, N. D., 2021. The role of detrital components in the petrophysical parameters of Paleogene calcareous-dominated hemipelagic deposits. Arabian Journal of Geosciences 14, 1027.

Pujalte, V., Baceta, J. I., Schmitz, B., 2015. A massive input of coarse-grained siliciclastics in the Pyrenean Basin during the PETM: The missing ingredient in a coeval abrupt change in hydrological regime. Climate of the Past 11, 1653–1672.

Reghellin, D., Coxall, H. K., Dickens, G. R., Backman, J., 2015. Carbon and oxygen isotopes of bulk carbonate in sediment deposited beneath the eastern equatorial Pacific over the last 8 million years. Paleoceanography 30, 1261–1286.

Romein, T., 1979. Lineages of early Paleogene calcareous nannoplankton. Utrecht Micropaleontological Bulletins 22.

Schmitz, B., Charisi, S. D., Thompson, E. I., Speijer, R. P., 1997. Barium, SiO_2 (excess), and P_2O_5 as proxies of biological productivity in the Middle East during the Palaeocene and the latest Palaeocene benthic extinction event. Terra Nova 9, 95–99.

Schmitz, B., Speijer, R. P., Aubry, M. P., 1996. Latest Paleocene benthic extinction event on the southern Teth-

yan shelf (Egypt): Foraminiferal stable isotopic ($\delta^{13}C$, $\delta^{18}O$) records. Geology 24, 347–350.

Schrag, D. P., DePaolo, D. J., Richter, F. M., 1995. Reconstructing past sea surface temperatures: Correcting for diagenesis of bulk marine carbonate. Geochimica et Cosmochimica Acta 59, 2265–2278.

Segev, A., Schattner, U., Lyakhovsky, V., 2011. Middle-Late Eocene structure of the southern Levant continental margin – Tectonic motion versus global sea-level change. Tectonophysics 499, 165–177.

Seton, M., Müller, R. D., Zahirovic, S., Gaina, C., Torsvik, T., Shephard, G., Talsma, A., Gurnis, M., Turner, M., Maus, S., Chandler, M., 2012. Global continental and ocean basin reconstructions since 200Ma. Earth-Science Reviews 113, 212–270.

Sexton, P. F., Norris, R. D., Wilson, P. A., Pälike, H., Westerhold, T., Röhl, U., Bolton, C. T., Gibbs, S., 2011. Eocene global warming events driven by ventilation of oceanic dissolved organic carbon. Nature 471, 349–353.

Sexton, P. F., Wilson, P. A., Pearson, P. N., 2006. Microstructural and geochemical perspectives on planktic foraminiferal preservation: "glassy" versus "frosty.". Geochemistry, Geophysics, Geosystems 7, Q12P19.

Shackleton, N. J., 1986. Paleogene stable isotope events. Palaeogeography, Palaeoclimatology, Palaeoecology 57, 91–102.

Shackleton, N. J., Hall, M. A., Bleil, U., 1985. Carbon-Isotope Stratigraphy, Site 577. Initial Reports of the Deep Sea Drilling Project 86, 503–511.

Shackleton, N. J., Hall, N., Boersma, A., 1984. Oxygen and Carbon Isotope Data from Leg 74 Foraminifers. Proceedings of the Ocean Drilling Program, Initial Reports 74, 559–612.

Shahar, J., 1994. The Syrian arc system: an overview. Palaeogeography, Palaeoclimatology, Palaeoecology 112, 125–142.

Sharland, P. R., Archer, R., Casey, D. M., Davies, R. B., Hall, S. H., Heward, A. P., Horbury, A. D., Simmons, M. D., 2001. Arabian Plate Sequence Stratigraphy, Gulf PetroLink, Bahrain.

Slotnick, B. S., Dickens, G. R., Hollis, C. J., Crampton, J. S., Percy Strong, C., Phillips, A., 2015. The onset of the Early Eocene Climatic Optimum at Branch Stream, Clarence River valley, New Zealand. New Zealand Journal of Geology and Geophysics 58, 262–280.

Slotnick, B. S., Dickens, G. R., Nicolo, M. J., Hollis, C. J., Crampton, J. S., Zachos, J., Sluijs, A., 2012. Large-amplitude variations in carbon cycling and terrestrial weathering during the latest Paleocene and earliest Eocene: The record at Mead Stream, New Zealand. Journal of Geology 120, 487–505.

Sluijs, A., Bowen, G. J., Brinkhuis, H., Lourens, L. J., Thomas, E., 2007. The Palaeocene-Eocene Thermal Maximum super greenhouse: Biotic and geochemical signatures, age models and mechanisms of global change. In: Williams, M., Haywood, A., Gregory, F., Schmidt, D. (Eds.), Deep-Time Perspectives on Climate Change: Marrying the Signal from Computer Models and Biological Proxies. The Micropalaeontoloigcal Society Special Publications, The Geological Society, London, 323–349.

Sluijs, A., Dickens, G. R., 2012. Assessing offsets between the $\delta^{13}C$ of sedimentary components and the global exogenic carbon pool across early Paleogene carbon cycle perturbations. Global Biogeochemical Cycles 26, GB4005.

Sluijs, A., Schouten, S., Donders, T. H., Schoon, P. L., Röhl, U., Reichart, G. J., Sangiorgi, F., Kim, J. H., Sinninghe Damsté, J. S., Brinkhuis, H., 2009. Warm and wet conditions in the Arctic region during Eocene Thermal Maximum 2. Nature Geoscience 2, 777–780.

Sluijs, A., Van Roij, L., Harrington, G. J., Schouten, S., Sessa, J. A., Levay, L. J., Reichart, G. J., Slomp, C. P., 2014. Warming, euxinia and sea level rise during the paleocene-eocene thermal maximum on the gulf coastal plain: Implications for ocean oxygenation and nutrient cycling. Climate of the Past 10, 1421–1439.

Speijer, R. P., 1994a. Extinction and recovery patterns in benthic foraminiferal paleocommunities across the Cretaceous/Paleogene and Paleocene/Eocene boundaries. Ph. D. Thesis, Utrecht University, Utrecht, Netherlands, 123 p.

Speijer, R. P., 1994b. The late Paleocene benthic foraminiferal extinction as observed in the Middle East. Bulletin – Societe Belge de Geologie 103, 267–280.

Speijer, R. P., Scheibner, C., Stassen, P., Morsi, A. M. M., 2012. Response of marine ecosystems to deep-time global warming: A synthesis of biotic patterns across the Paleocene-Eocene thermal maximum (PETM). Austrian Journal of Earth Sciences 105, 6–16.

Speijer, R. P., Schmitz, B., 1998. A benthic foraminiferal record of Paleocene sea level and trophic/redox conditions at Gebel Aweina, Egypt. Palaeogeography, Palaeoclimatology, Palaeoecology 137, 79–101.

Speijer, R. P., Wagner, T., 2002. Sea-level changes and black shales associated with the late Paleocene thermal maximum: Organic-geochemical and micropaleontologic evidence from the southern Tethyan margin (Egypt-Israel). Special Paper of the Geological Society of America 356, 533–549.

Stap, L., Lourens, L. J., Thomas, E., Sluijs, A., Bohaty, S., Zachos, J., 2010. High-resolution deep-sea carbon and oxygen isotope records of Eocene Thermal Maximum 2 and H2. Geology 38, 607–610.

Stap, L., Sluijs, A., Thomas, E., Lourens, L. J., 2009. Patterns and magnitude of deep sea carbonate dissolution during Eocene Thermal Maximum 2 and H2, Walvis Ridge, southeastern Atlantic Ocean. Paleoceanography 24, PA1211.

Staudigel, P. T., Swart, P. K., 2019. A diagenetic origin for isotopic variability of sediments deposited on the margin of Great Bahama Bank, insights from clumped isotopes. Geochimica et Cosmochimica Acta 258, 97–119.

Stoll, H. M., 2005. Limited range of interspecific vital effects in coccolith stable isotopic records during the Paleocene-Eocene thermal maximum. Paleoceanography 20, PA1007.

Swart, P. K., 2008. Global synchronous changes in the carbon isotopic composition of carbonate sediments unrelated to changes in the global carbon cycle. Proceedings of the National Academy of Sciences of the United States of America 105, 13741–13745.

Swart, P. K., Mackenzie, G. J., Eberli, G. P., Lüdmann, T., Betzler, C., 2019. Do drifts deposited adjacent to carbonate platforms record the signal of global carbon isotopic values? Sedimentology 66, 1410–1426.

Thomas, E., Zachos, J., 2000. Was the late Paleocene thermal maximum a unique event? Geologiska Föreningens i Stockholm Förhandlingar 122, 169–170.

Torsvik, T. H., Van der Voo, R., Preeden, U., Mac Niocaill, C., Steinberger, B., Doubrovine, P. V., van Hinsbergen, D. J. J., Domeier, M., Gaina, C., Tohver, E., Meert, J. G., McCausland, P. J. A., Cocks, L. R. M., 2012. Phanerozoic Polar Wander, Palaeogeography and Dynamics. Earth-Science Reviews 114, 325–368.

Verosub, K. L., Roberts, A. P., 1995. Environmental magnetism – Past, present, and future. Journal of Geophysical Research 100, 2175–2192.

Weinbaum-Hefetz, M., 20013. Nannofossil Assemblages and Palaeoceanography of the Eocene Levant Margin of Israel. Ph. D. Thesis, Ben-Gurion University of the Negev, Beersheba, Israel (In Hebrew).

Weinbaum-Hefetz, M., Benjamini, C., 2011. Calcareous nannofossil assemblage changes from early to middle Eocene in the Levant margin of the Tethys, central Israel. Journal of Micropalaeontology 30, 129–139.

Westerhold, T., Marwan, N., Drury, A. J., Liebrand, D., Agnini, C., Anagnostou, E., Barnet, J., Bohaty, S. M., De Vleeschouwer, D., Florindo, F., Frederichs, T., Hodell, D. A., Holbourn, A. E., Kroon, D., Lauretano, V., Littler, K., Lourens, L. J., Lyle, M., Pälike, H., Röhl, U., Tian, J., Wilkens, R. H., Zachos, J. C., 2020. An astronomically dated record of Earth's climate and its predictability over the last 66 million years. Science 369, 1383–1388.

Westerhold, T., Röhl, U., Donner, B., McCarren, H., Zachos, J., 2011. A complete high-resolution Paleocene benthic stable isotope record for the central Pacific (ODP Site 1209). Paleoceanography 26, PA2216.

Westerhold, T., Röhl, U., Donner, B., Zachos, J., 2018. Global Extent of Early Eocene Hyperthermal Events: A New Pacific Benthic Foraminiferal Isotope Record From Shatsky Rise (ODP Site 1209). Paleoceanography and Paleoclimatology 33, 626–642.

Westerhold, T., Röhl, U., Frederichs, T., Agnini, C., Raffi, I., Zachos, J., Wilkens, R. H., 2017. Astronomical calibration of the Ypresian timescale: Implications for seafloor spreading rates and the chaotic behavior of the solar system? Climate of the Past 13, 1129–1152.

Zachos, J., Dickens, G. R., Zeebe, R. E., 2008. An early Cenozoic perspective on greenhouse warming and carbon-cycle dynamics. Nature 451, 279–283.

Zachos, J., McCarren, H., Murphy, B., Röhl, U., Westerhold, T., 2010. Tempo and scale of late Paleocene and early Eocene carbon isotope cycles: Implications for the origin of hyperthermals. Earth and Planetary Science Letters 299, 242–249.

Zachos, J., Pagani, H., Sloan, L., Thomas, E., Billups, K., Pagani, M., Sloan, L., Thomas, E., Billups, K., 2001. Trends, rhythms, and aberrations in global climate 65 Ma to present. Science 292, 686–693.

Zachos, J., Röhl, U., Schellenberg, S. A., Sluijs, A., Hodell, D. A., Kelly, D. C., Thomas, E., Nicolo, M., Raffi, I., Lourens, L. J., McCarren, H., Kroon, D., 2005. Paleoclimate: Rapid acidification of the ocean during the paleocene-eocene thermal maximum. Science 308, 1611–1615.

Zachos, J., Stott, L. D., Lohmann, K. C., 1994. Evolution of Early Cenozoic marine temperatures. Paleoceanography 9, 353–387.

Zeebe, R. E., Lourens, L. J., 2019. Solar System chaos and the Paleocene–Eocene boundary age constrained by geology and astronomy. Science 365, 926–929.

Ziegler, M., 2001. Late Permian to Holocene paleofacies evolution of the Arabian Plate and its hydrocarbon occurrences. GeoArabia 6, 445–505.

Manuscript received: May 21, 2021
Revisions required: August 31, 2021
Revised version received: October 14, 2021
Manuscript accepted: October 26, 2021

Appendix

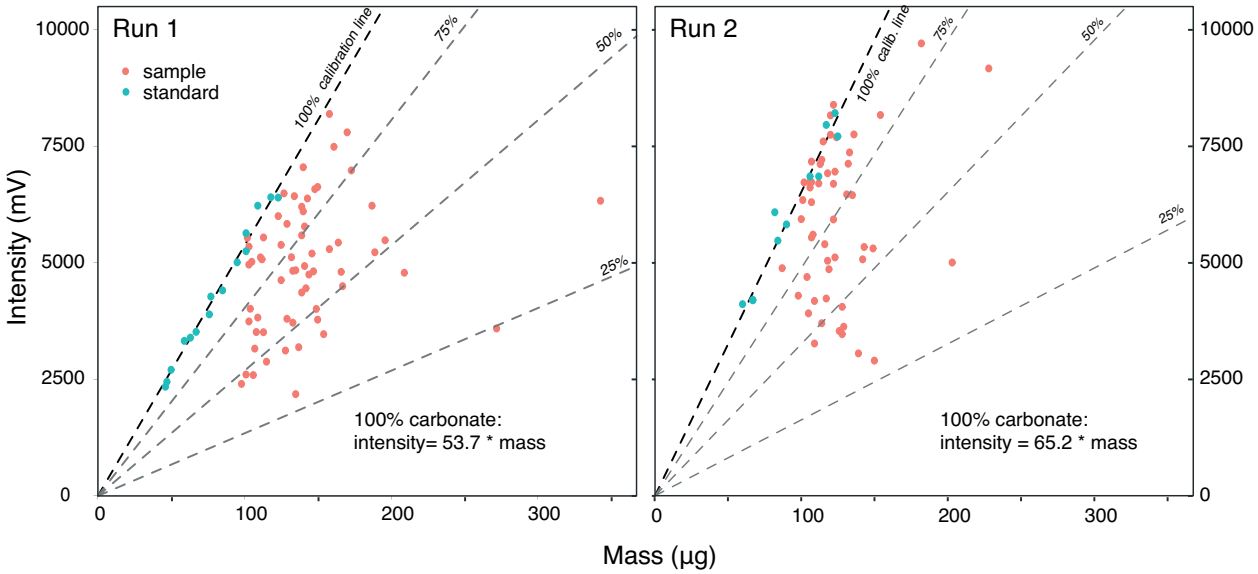

Fig. S1. Visualization of wt%$CaCO_3$ calculation. Sample weight (µg) versus peak *m/z* 44 intensity (mV) measured on the Thermo Delta-V mass-spectrometer for run 1 (left) and run 2 (right). Red dots represent measured samples. The blue dots represent the measured samples, with the black-dashed line as the linear regression model through the carbonate standards, with formula and R_2 on the top left. Grey-dashed lines mark the slopes of 25.50 and 75 % carbonate relative to the 100 % calibration line.

Table S1. List of analyzed core RH-323 sample depths together with bulk isotope and MS results

Sample bottom depth (mbs)	$\delta^{13}C$ (‰, VPDB)	$\delta^{18}O$ (‰, VPDB)	Magnetic susc. (χ)	Sample bottom depth (mbs)	$\delta^{13}C$ (‰, VPDB)	$\delta^{18}O$ (‰, VPDB)	Magnetic susc. (χ)
92.98	0.36	–2.38	3.67E-09	174.30	0.96	–3.06	6.73E-10
96.68	0.21	–2.39	8.87E-10	177.60	0.80	–2.89	1.59E-09
99.80	0.51	–2.14	6.78E-09	180.80	0.83	–2.74	3.74E-09
103.00	0.82	–2.06	4.57E-09	183.80	0.46	–2.88	3.66E-09
106.35	0.49	–2.65	3.79E-10	184.58	0.54	–2.46	1.05E-08
109.80	0.20	–2.85	1.77E-09	187.16	–0.42	–3.52	3.38E-09
113.00	0.60	–2.42	1.03E-09	190.45	0.46	–3.01	2.21E-09
115.42	0.19	–3.02	–4.61E-10	193.70	0.38	–2.90	1.43E-09
119.50	0.05	–3.38	8.03E-10	197.07	0.24	–2.96	6.00E-09
120.95	0.54	–2.55	–1.94E-09	200.30	0.65	–2.14	1.90E-08
126.50	–0.02	–2.66	2.34E-09	203.20	0.53	–2.89	3.54E-09
128.50	0.18	–2.99	–2.22E-10	208.22	0.85	–2.86	1.02E-08
132.00	0.88	–2.31	4.63E-09	210.10	0.47	–3.13	1.69E-09
135.00	0.44	–2.84	5.68E-10	211.70	0.39	–3.22	2.23E-09
138.20	0.50	–2.14	6.74E-09	215.00	0.71	–3.01	1.38E-09
141.20	0.70	–2.95	–3.88E-10	219.80	0.59	–3.24	2.12E-09
147.10	0.97	–2.35	1.53E-09	226.45	–0.02	–3.62	5.36E-09
151.35	1.11	–2.10	2.08E-09	227.23	0.20	–3.21	1.89E-09
154.00	1.11	–2.24	3.84E-10	232.08	0.03	–2.48	7.53E-09
157.75	0.76	–2.83	–6.18E-10	232.50	0.13	–3.44	1.95E-08
160.45	0.90	–2.73	7.58E-10	236.70	0.13	–3.19	1.01E-08
164.30	0.42	–2.94	6.79E-10	240.10	0.22	–1.92	2.20E-08
167.70	1.13	–1.80	9.92E-09	242.70	–0.23	–3.10	2.87E-09
170.70	0.84	–2.55	6.43E-09	246.70	–0.12	–2.39	6.34E-09

Sample bottom depth (mbs)	$\delta^{13}C$ (‰, VPDB)	$\delta^{18}O$ (‰, VPDB)	Magnetic susc. (χ)
250.05	–0.45	–3.35	3.49E-08
253.25	–0.14	–2.76	4.76E-09
254.85	–0.36	–2.68	6.01E-09
260.15	0.24	–2.31	3.67E-08
263.60	0.09	–2.87	1.29E-08
266.93	–0.12	–2.53	1.07E-08
270.06	0.10	–2.42	1.09E-09
273.38	–0.23	–2.68	1.17E-08
276.55	0.05	–2.57	3.29E-08
283.05	0.41	–2.57	3.94E-08
286.52	0.31	–2.71	4.59E-08
289.74	0.71	–2.75	4.63E-08
292.86	0.83	–2.86	3.89E-08
296.20	0.78	–2.76	7.94E-08
297.15	1.48	–2.59	7.92E-08
298.25	1.63	–2.87	5.78E-08
299.05	1.00	–3.13	6.69E-08
299.80	0.32	–2.68	2.77E-08
299.95	1.21	–3.05	5.91E-08
301.05	1.19	–2.89	8.15E-08
302.34	1.26	–2.83	7.48E-08
303.10	1.18	–2.96	6.58E-08
304.40	1.29	–2.93	6.34E-08
309.00	–1.16	–4.21	5.05E-08
309.40	1.85	–2.66	8.43E-08
312.24	1.95	–2.69	6.41E-08
318.20	2.13	–2.36	8.14E-08
321.35	2.06	–2.60	5.44E-08
322.00	1.99	–2.74	3.72E-08
322.50	2.09	–2.60	4.82E-08
323.00	2.18	–2.47	5.77E-08
323.50	2.20	–2.58	3.97E-08
324.05	1.96	–2.54	6.42E-08
324.50	2.10	–2.37	6.59E-08
325.00	1.96	–2.65	3.86E-08
325.50	2.10	–2.21	6.55E-08
326.60	1.88	–2.61	2.75E-08
327.00	2.24	–2.49	3.20E-08
327.55	1.98	–2.32	5.07E-08
328.10	2.20	–2.19	5.76E-08
328.50	1.97	–1.97	7.03E-08
328.95	2.42	–2.28	4.57E-08
329.25	2.46	–2.53	4.51E-08
329.50	2.65	–2.33	2.00E-08
330.50	2.61	–2.35	1.45E-08
331.00	2.52	–2.29	1.16E-08
331.50	2.69	–2.28	1.55E-08
332.50	2.23	–2.38	3.18E-08
333.75	1.75	–1.99	5.17E-08
334.00	1.81	–2.25	3.60E-08
334.45	1.95	–2.13	3.60E-09
334.95	1.77	–2.32	1.64E-08
335.45	2.05	–2.35	1.59E-08
336.00	1.90	–2.07	2.03E-08
336.45	2.06	–2.02	4.19E-08
337.00	1.99	–2.20	3.82E-08
337.55	1.85	–2.39	2.21E-08
338.05	2.61	–2.42	1.76E-08
338.10	2.18	–2.27	4.45E-08
338.50	2.28	–2.25	4.71E-08
339.50	1.66	–2.26	4.37E-08
340.10	1.68	–2.27	3.75E-08
340.60	1.82	–2.38	2.41E-08
341.00	1.86	–2.05	3.23E-08
342.60	1.78	–2.25	6.63E-08
343.70	1.56	–2.24	6.91E-08
344.76	1.51	–2.08	3.94E-08

Table S2a. Calcareous nannoplankton biostratigraphy of Core RH-323. Calcareous nannofossil biostratigraphy of Core RH-323 following the work of Eshet and Siman-Tov (2000). The ages of the bioevents are calculated using the mentioned age reference and magnetochron ages of GPTS 2012 (Gradstein et al. 2012), modified with the astronomical calibrated Ypresian by Westerhold et al. (2017).

Depth (mbs)	Type event	Species	Biozone	Age (Ma)	Age reference
225	LO	*Tribrachiatus orthostylus*	Top NP 12	50.658	Agnini et al. 2006
265	FO	*Discoaster lodoensis*	Base NP 12	53.014	Agnini et al. 2006
287	LO	*Tribrachiatus contortus*	Base NP 11	54.266	Agnini et al. 2006
287	FO	*Tribrachiatus orthostylus*	Top NP 10	54.258	Agnini et al. 2006
300	FO	*Tribrachiatus bramlettei*	Base NP 10	55.422	Agnini et al. 2006
325	FCO	*Discoaster multiradiatus*	Base NP 9	57.223	Agnini et al. 2007
338	FO	*Discoaster mohleri*	Base NP 7	58.974	Agnini et al. 2007

Table S3b. Planktonic foraminifer biostratigraphy of Core RH-323. Planktonic foraminifer biostratigraphy of Core RH-323 following the work of Eshet and Siman-Tov (2000). The ages of the bioevents are calculated using the referred age reference and magnetochron ages of GPTS 2012 (Gradstein et al. 2012), modified with the astronomical calibrated Ypresian by Westerhold et al. (2017).

Depth (mbs)	Type	Species	Biozone	Age (Ma)	Age reference
250	LO	*Morozovella aequa*	Top P7	53.586	Berggren et al. 1995
250	FO	*Acarinina pentacamerata*	Base P8	52.644	Luciani and Giusberti 2014
250	FO	*Acarinina bullbrooki*	Base P8	50.561	Luciani and Giusberti 2014
269	FO	*Morozovella aragonensis*	Base P7	53.360	Luciani and Giusberti 2014
283	LO	*Morozovella velascoensis*	Top P5	55.668	Luciani and Giusberti 2014
306	LO	*Globanomalina pseudomenardii*	Top P4	57.095	Berggren et al. 1995
306	LO	*Acarinina mckannai*	Top P4	57.555	Berggren et al. 1995